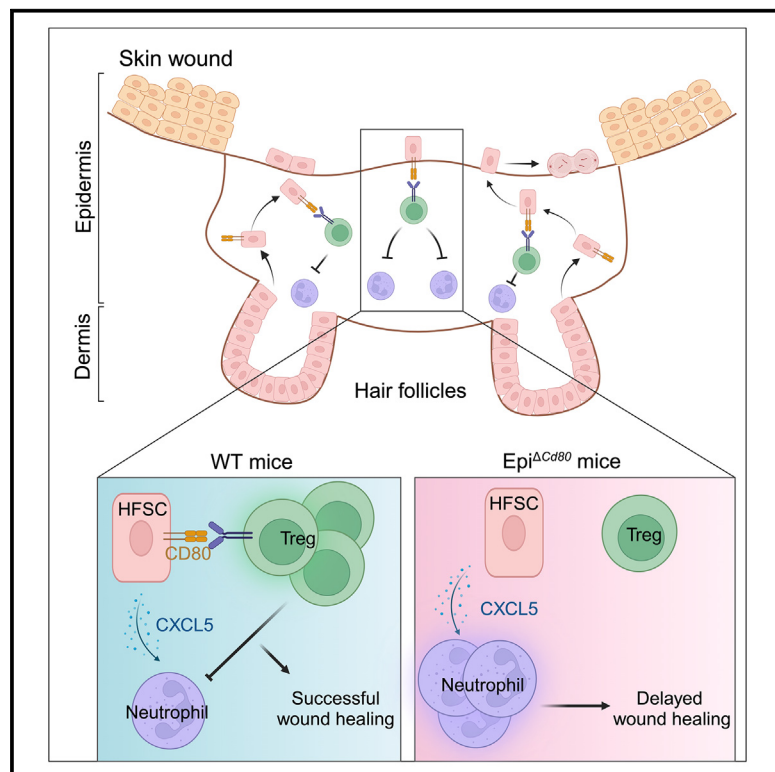


Immunity

CD80 on skin stem cells promotes local expansion of regulatory T cells upon injury to orchestrate repair within an inflammatory environment

Graphical abstract



Authors

Jingyun Luan, Cynthia Truong,
Aleksandra Vuchkovska, ...,
Alexander Y. Rudensky, Elaine Fuchs,
Yuxuan Miao

Correspondence

fuchslb@rockefeller.edu (E.F.),
miaoy@uchicago.edu (Y.M.)

In brief

In skin injury, the inflammatory environment can impact repair mediated by skin stem cells. Luan, Truong, Vuchkovska, et al. show that hair follicle stem cells migrate into the wound, activate immune-modulatory molecules, and expand extrathymic regulatory T cells to facilitate the resolution of neutrophil responses and the initiation of wound repair.

Highlights

- Migrating HFSCs activate CD80 during cutaneous wound repair
- CD80 deficiency in HFSCs causes delayed wound healing
- HFSCs acquire CD80 to expand extrathymic regulatory T cells
- HFSC and Treg cell interactions prevent accumulation of neutrophils



Article

CD80 on skin stem cells promotes local expansion of regulatory T cells upon injury to orchestrate repair within an inflammatory environment

Jingyun Luan,^{1,5} Cynthia Truong,^{2,5} Aleksandra Vuchkovska,^{1,5} Weijie Guo,¹ Jennifer Good,¹ Bijun Liu,¹ Audrey Gang,¹ Nicole Infarinato,² Katherine Stewart,² Lisa Polak,² Hilda Amalia Pasolli,³ Emma Andretta,⁴ Alexander Y. Rudensky,⁴ Elaine Fuchs,^{2,5,6,*} and Yuxuan Miao^{1,5,6,7,*}

¹Ben May Department of Cancer Research, The University of Chicago, Chicago, IL 60615, USA

²Howard Hughes Medical Institute, Robin Chemers Neustein Laboratory of Mammalian Development and Cell Biology, The Rockefeller University, New York, NY 10065, USA

³Electron Microscopy Resource Center, The Rockefeller University, New York, NY 10065, USA

⁴Howard Hughes Medical Institute, Immunology Program, Sloan Kettering Institute, Memorial Sloan Kettering Cancer Center, New York, NY 10065, USA

⁵These authors contributed equally

⁶Senior author

⁷Lead contact

*Correspondence: fuchs@rockefeller.edu (E.F.), miaoy@uchicago.edu (Y.M.)

<https://doi.org/10.1016/j.immuni.2024.04.003>

SUMMARY

Following tissue damage, epithelial stem cells (SCs) are mobilized to enter the wound, where they confront harsh inflammatory environments that can impede their ability to repair the injury. Here, we investigated the mechanisms that protect skin SCs within this inflammatory environment. Characterization of gene expression profiles of hair follicle SCs (HFSCs) that migrated into the wound site revealed activation of an immune-modulatory program, including expression of CD80, major histocompatibility complex class II (MHCII), and CXC motif chemokine ligand 5 (CXCL5). Deletion of CD80 in HFSCs impaired re-epithelialization, reduced accumulation of peripherally generated Treg (pTreg) cells, and increased infiltration of neutrophils in wounded skin. Importantly, similar wound healing defects were also observed in mice lacking pTreg cells. Our findings suggest that upon skin injury, HFSCs establish a temporary protective network by promoting local expansion of Treg cells, thereby enabling re-epithelialization while still kindling inflammation outside this niche until the barrier is restored.

INTRODUCTION

Adult stem cells (SCs) are responsible for maintaining and regenerating body tissues.¹ Indispensable and long-lived, tissue SCs are challenged by frequent exposure to inflammation caused by a myriad of infections and injuries over a plant's or animal's lifetime.^{2–4} Facing such challenges, SCs must be protected from repeated bouts of inflammation to ensure rapid tissue regeneration while also maintaining the SC pool for tissue homeostasis and for confronting future injuries. Despite this vital necessity, it is unclear how adult SCs survive and drive tissue regeneration within the inflammatory environment that ensues following injury.

Mammalian skin offers an excellent system to tackle this question. During homeostasis, epithelial SCs of the skin reside within specialized niches that receive inputs from their local microenvironments to instruct them what to do and when.⁵ Epidermal SCs (EpSCs) reside within the innermost (basal) layer of the skin epithelium, where they are responsible for making and replenish-

ing the surface barrier that retains body fluids and excludes harmful microbes. Additional skin epithelial SCs reside within local niches of epidermal appendages, including sebaceous glands, sweat glands, and hair follicles (HFs). These epithelial SCs share a common embryonic precursor. In the adult, they are typified by keratins 5 (K5) and 14 (K14) and reside along a contiguous basement membrane, which demarcates the epithelium from the dermis and is rich in extracellular matrix and growth factors. Along the basement membrane are distinct niches that are uniquely tailored to suit the specialized tasks of each SC population, enabling them to regenerate and rejuvenate the epithelium within their particular domain.⁶

Upon injury, skin epithelial SCs become mobilized to leave the confines of their native niches. Whether it is the SCs of the epidermis or an epidermal appendage, once they are called into action and exit the confines of their native niches, they are unleashed to perform a new task, namely re-epithelialization of damaged tissue.^{7–12} An excellent example of this phenomenon takes place in frequently occurring shallow skin wounds, where



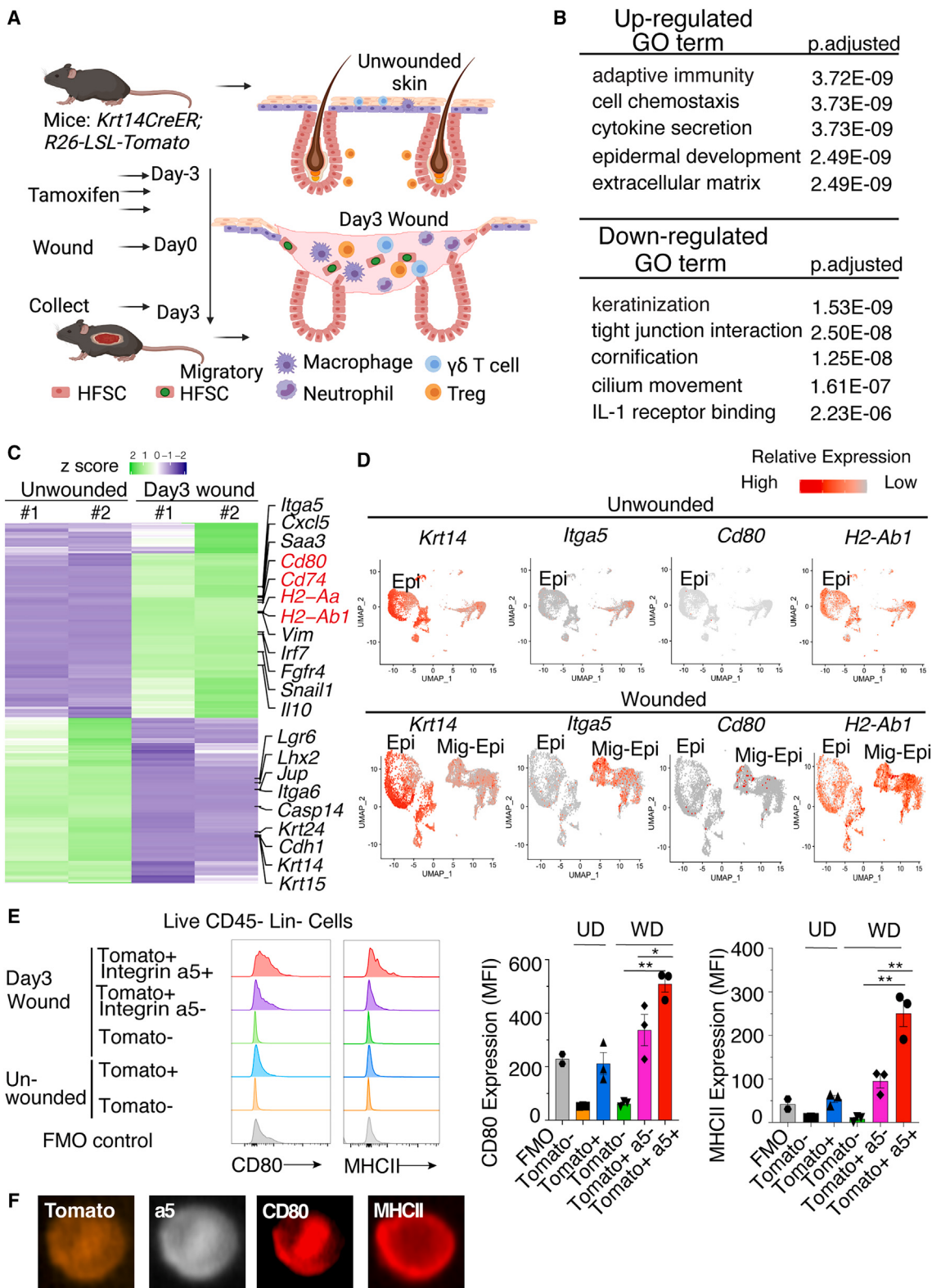


Figure 1. Skin epithelium activates an immune-modulatory program during wound healing

(A) Schematic showing the lineage tracing of basal skin epithelium, followed by partial-thickness wounding.

(B) Gene Ontology analysis of differentially expressed genes in basal skin keratinocytes from wounded skin (day 3 wound) compared with cells from unwounded skin.

(legend continued on next page)

the skin has been denuded of the epidermis and the upper non-cycling portion of the HF. This forces the underlying HFSCs residing in an anatomical structure called the bulge to be repurposed from their normal hair regeneration role to instead migrate upward and repair the damaged epithelial tissue.¹³ The newly repaired epidermis is thus composed of former HFSCs that now act as EpdSCs, maintaining the skin barrier and guarding against infections.⁶

Under homeostasis, SCs are often thought to reside within an immune-privileged environment.^{14,15} Although the field is still evolving, it has been postulated that the SC niche of the HF bulge maintains immune privilege by producing immunosuppressive molecules such as interleukin-10 (IL-10) or transforming growth factor β (TGF- β) to dampen inflammation around the SCs if homeostasis is perturbed.^{16,17} It has been further suggested that suppressive immune cells such as tissue-resident regulatory T cells (Treg cells) may even play an active role during normal skin homeostasis, where they have been implicated in stimulating self-renewal and promoting hair regeneration in the normal hair cycle.^{18,19}

A major unaddressed question is how SCs are protected following injury when they leave their niche and migrate into the wound bed to restore the barrier.⁶ After wounding, damaged tissue is exposed to pathogens and dead cells, triggering a cascade of responses that includes the recruitment of inflammatory immune cells such as neutrophils (Neu), monocytes (Mo), and macrophages (MACs), which secrete not only anti-microbial molecules but also pro-inflammatory cytokines. These factors are critical for fending off pathogens and clearing dead cells, but if left unchecked, they can cause immense stress for the SCs. Caught in the crosshairs of such robust inflammation outside of their immune-privileged niche, adult SCs must be poised to evade collateral damage from infiltrating inflammatory immune cells so they can successfully re-epithelialize the wound.

Here, we explored this possibility and interrogated the behavior of skin SCs in a mouse model of partial-thickness skin wounding in which injury-activated HFSCs migrated out of their bulge niche and entered the highly inflammatory wound bed to regenerate the damaged epidermis and upper HF.

RESULTS

HFSCs activate immune-modulatory programs during wound repair

Partial-thickness wounding mechanically removes the superficial epidermis and upper HF, leaving intact the dermal components, including the epithelial SC niche of the HF (Figure 1A).^{2,13} To broadly examine how skin epithelium reacts to wound-induced inflammation, we began by using *Krt14CreER*; *Rosa26-LSL-*

tdTomato mice to trace the progeny of basal keratinocytes in the mouse skin, which contain both interfollicular EpdSCs and HFSCs. Following tamoxifen administration to activate *tdTomato* expression, we administered a shallow wound with a calibrated Dremel tool at day 0, then waited 3 days until the migrating HFSCs had entered the wound bed (Figure 1A). We then prepared single-cell suspensions of the skins and used fluorescence-activated cell sorting (FACS) to isolate *tdTomato*⁺ epithelial cells. After excluding immune cells (*CD45*⁺), endothelial cells (*CD31*⁺), fibroblasts/adipocytes (*CD140a*⁺), and melanocytes (*CD117*⁺), we further screened for integrin $\alpha 5$, a marker of wound-activated, migrating epithelial cells (Figure S1A).²

When we subjected the pool of FACS-isolated integrin $\alpha 5$ ⁺ *tdTomato*⁺ epithelial cells to RNA sequencing (RNA-seq), we observed good concordance between replicates (Figure S1B). As reflected in the Gene Ontology (GO) analysis, transcripts encoding keratinization and differentiation characteristics were among the most downregulated, while upregulated transcripts encoded putative extracellular matrix and migration-associated proteins as well as secreted cytokines (Figure 1B).

Of particular interest were transcripts involved in antigen presentation and immune co-stimulation (e.g., *Cd74*, *H2-Aa*, *H2-Ab1*, and *Cd80*), which were induced in the injury-activated epithelial SCs that had migrated into the wound bed (Figure 1C). Although MHCII molecules and CD80 are classical features of dendritic cells (DCs) and MACs, MHCII has recently been found on the surface of neural progenitors, intestinal epithelial SCs, ductal cells, and some tumor cells, while CD80, a member of the B7 family molecules, has been reported in the tumor-initiating SCs of various epithelial cancers.^{20–25} In immune cells, these proteins are known to modulate immune responses by activating T cell receptor (TCR) signaling and providing co-stimulatory signals to T lymphocytes. This leads to the tantalizing hypothesis that tissue SCs that move into the wound bed have the capacity to modulate T cells.

Probing deeper into this possibility, we analyzed the single-cell transcriptome of cells isolated from full-thickness skin wounds and confirmed the immune-modulatory feature of our *CD45*^{neg}*K14*⁺ epithelial cells.²⁶ We showed that the transcripts for *Cd80* and MHCII components were exclusive to a subset of skin keratinocytes that emerged after wounding and exhibited classical features of having undergone a partial epithelial-mesenchymal transition and activated migration (*Itga5*, *Vim*, and *Snail*), accompanied by dampened epithelial features (*Krt14*, *Krt5*, and *Cdh1*) (Figures 1D and S1C). Even within this migratory epithelial population, the transcriptional activation status of *Cd80* was heterogeneous, with only a small subset (less than 10%) of total *Krt14*⁺*Itga5*⁺ cells expressing appreciable levels of the mRNA encoding this immune-modulatory factor.

(C) Heatmap and representative genes that are differentially expressed in basal skin keratinocytes from wounded skin (day 3 wound) compared with cells from unwounded skin.

(D) Uniform manifold approximation and projection (UMAP) plots showing expression of various markers, including *Cd80* and MHCII genes, activated in the basal epithelial skin cells during wound repair.

(E) Flow cytometry plots and median fluorescence intensity (MFI) quantification of CD80 and MHCII on various cell populations in unwounded (UD) or wounded (WD) skin. Each symbol represents an independent animal. Representative data from three independent experiments are shown as mean \pm SEM. Unpaired t test; * $p < 0.05$, ** $p < 0.01$. See also Figure S1.

(F) ImageStream analysis to visualize co-expression of CD80 and MHCII in the *Tomato*⁺ basal epithelial SCs that have acquired integrin $\alpha 5$ ⁺ and migrated into the wounded skin (day 3 wound).

Based upon these observations, we compared the gene signatures of *Cd80⁺Igfa5⁺* and *Cd80^{neg}Igfa5⁺* epithelial cells and found that, compared with the *Cd80^{neg}* cells, the *Cd80⁺* migratory epithelial cells expressed a higher level of additional immune-modulatory factors or cytokines, such as *CD74*, *H2-Aa*, *Il1b*, and *Ccl3* (Figure S1D). As these features are typically ones of immune cells rather than epithelial cells, we further confirmed these findings at the protein level by performing flow cytometry analysis on migratory epithelial skin SCs isolated on day 3 post-wounding from *Krt14CreER; Rosa26-LSL-tdTomato* mice, which had been activated for lineage-tracing during the telogen-phase of the hair cycle (see Figure 1A). These data showed that individual migratory epithelial skin SCs in the wound bed, which were marked by K14 (*Krt14CreER*-induced tdTomato) and α 5 integrin concomitantly displayed surface CD80 and MHCII (Figure 1E). Their selective coactivation in wound-induced skin SCs was further exemplified by image stream analyses of individual SCs (Figure 1F). Notably, these markers were not detected in unwounded epithelial skin SCs, nor were they found in other non-immune cell populations within the wounded skin (Figure 1E).

Previous lineage-tracing experiments have demonstrated that, when the epidermis and upper HF segments are removed in a partial-thickness wound, the underlying bulge HFSCs are the major SC population that migrate out of their niches and into the wound bed to repair the missing epithelial tissue.^{2,13} These HFSCs are the critical basal epithelial cells that undergo a partial epithelial-to-mesenchymal transition and acquire the migratory integrin α 5 to initiate re-epithelialization. By using *Sox9CreER; Rosa26-LSL-tdTomato* mice to specifically lineage trace HFSCs and not EpdSCs, we confirmed their contribution and kinetics in repairing the partial-thickness wound (Figure 2A; see also Gonzales et al.²).

Importantly, when lineage tracing of the *Sox9⁺* HF cells was activated prior to wounding and then analyzed on day 3 post-wounding, it was clear that the migrating α 5⁺tdTomato⁺ epithelial SCs in the wound bed were positive for CD80 (Figure 2B). Again, flow cytometry and image stream analyses of wound-induced epithelial SCs confirmed that, like the *Krt14CreER* lineage-traced cells, *Sox9CreER*-traced cells co-expressed markers of migrating HF-derived, and epithelial SCs and immunomodulatory cells were negative for the pan-immune cell marker CD45 (Figures 2C and 2D).

Using assay for transposase-accessible chromatin with sequencing (ATAC-seq), we analyzed the chromatin accessibility of HFSCs isolated from unwounded and wounded skin on day 3 post-wounding. Our data confirmed that the promoter region of both *Cd80* and MHCII genes in HFSCs, while present in an open chromatin state in normal skin homeostasis, gained prominent new open chromatin peaks upon wounding (Figure 2E). These data further bolstered the activation of immune-modulatory genes in wound-induced migratory HFSCs.

CD80 expressed by wound-activated skin SCs is essential to repair cutaneous wounds

To test the functional significance of the immune-modulatory program for skin epithelial SCs during wound repair, we took advantage of our finding that the migrating HFSCs are the major

non-hematopoietic cells expressing CD80 in wounded skin (Figure 2C). We therefore reconstituted lethally irradiated *Cd80* null mice with wild-type (WT) bone marrow (BM) and generated BM chimeras (*Cd80*^{-/-} mice with WT BM). In these mice, CD80 was expressed in the BM-derived immune cells but remained ablated in non-hematopoietic cells, notably HFSCs. To account for possible effects arising from the manipulations, WT control mice were also irradiated and reconstituted with the same WT BM (WT mice with WT BM).

1 day post-wounding, the skins of both cohorts displayed the eschar (scab) but remained denuded of its underlying epidermis. By day 3 post-wounding, the re-epithelialization process had been initiated in both WT and *Cd80* null mice harboring WT BMs (Figure 3A). By day 5 post-wounding, the wounds in the control group (WT mice with WT BM) were completely re-epithelialized with new hyperproliferative and differentiating K14⁺ epithelial cells covering the wound bed. In striking contrast, the *Cd80* null mice reconstituted with a WT hematopoietic system displayed only discrete portions of re-epithelialization, with large areas consisting of only granulated tissue (see quantifications in Figure 3A). Additionally, and again in contrast to the control mice, *Cd80* null mice with WT BM exhibited signs of a markedly delayed epidermal differentiation program with fewer newly generated K10⁺ barrier epidermal cells at day 5 of the repair process (Figure 3A).

To further interrogate the functional relevance to wound repair of CD80's expression by skin SCs and rule out possible contributions to the phenotype by resident *Cd80* null immune cells or other stromal populations remaining in the tissue after irradiation, we sought to design models to explicitly silence CD80 in the skin epithelium of otherwise WT mice. For this purpose, we employed a powerful ultrasound-guided *in utero* delivery strategy to achieve skin epithelium-specific CRISPR gene editing. In this approach, lentiviral (LV) particles are injected into the amniotic fluid of embryonic day 9.5 (E9.5) living mouse embryos to stably and selectively transduce the single-layered surface progenitors that later develop into the skin epithelium.²⁷ Using this method, we delivered an LV containing a single guide RNA (sgRNA) targeting *Cd80* *in utero* into *Krt14Cre; Rosa26-LSL-Cas9* mouse embryos to generate skin epithelial-specific *Cd80* knockout mice (Epi^{iCd80}) (Figure 3B). As K14Cre is activated by ~E14.5 and specific to the basal skin progenitors where the nascent HFSCs reside at this time, this ensured that CRISPR-Cas9-mediated gene editing and silencing of CD80 was activated only in the skin epithelium, leaving the CD80 in immune cells or any other stromal cells intact.

Given that the injected LV also carries a red fluorescent protein (RFP), we first imaged the transduced skin and confirmed good coverage (Figure S2A). Using qPCR and flow cytometry, we observed that at both RNA and protein levels, epithelial CD80 expression was diminished by >80% (Figures S2B and S2C). In order to control for potential impacts of skin microbiota affecting wound healing, we used littermates transduced with the same sgRNA targeting *Cd80* but without Cre (needed to activate Cas9 expression). Because Cre has toxicity in mammalian cells, we confirmed that Cre alone and without *Cd80* sgRNA LV did not affect re-epithelialization or differentiation (Figures S2D and S2E).

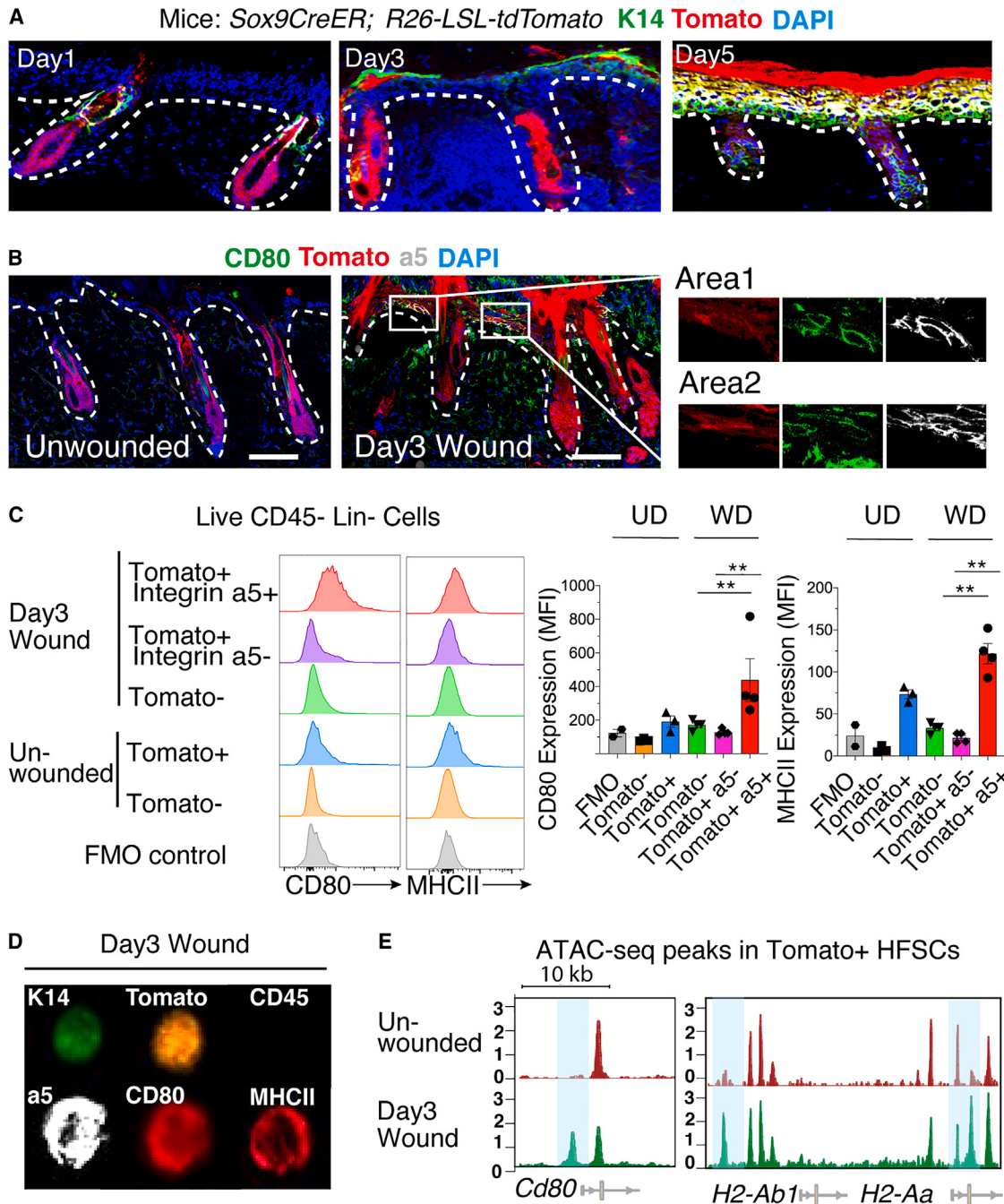


Figure 2. CD80 is activated in a subset of HFSCs that enter the wound bed during wound repair

- (A) Immunofluorescence (IF) images of sagittal sections of partial-thickness wounds showing the healing dynamics of *Sox9*⁺ HFSCs that were lineage-traced in *Sox9-CreER; Rosa26-tdTomato* mice. Scale bars, 100 μ m.
- (B) IF images of sagittal sections of unwounded or wounded (day 3) skin showing that Tomato⁺ HFSC cells that acquire a5 are also positive for CD80. Scale bars, 100 μ m.
- (C) Flow cytometry analysis and MFI quantification of CD80 and MHCII on various cell populations in unwounded (UD) or wounded (WD) skin. Each symbol represents an independent animal. Representative data from three independent experiments are shown as mean \pm SEM. Unpaired t test, ** p < 0.01.
- (D) ImageStream analysis to visualize CD80 and MHCII on migratory Tomato⁺ a5⁺ HFSCs from wounded skin (day 3 wound) on *Sox9CreER*-traced mice.
- (E) ATAC-seq peaks showing the accessibility status of the *Cd80* and MHCII (*H2-Aa* and *H2-Ab1*) genomic loci within the chromatin of FACS-purified, *Sox9CreER*-lineage-traced HFSCs from unwounded or wounded skin (day 3 wound).

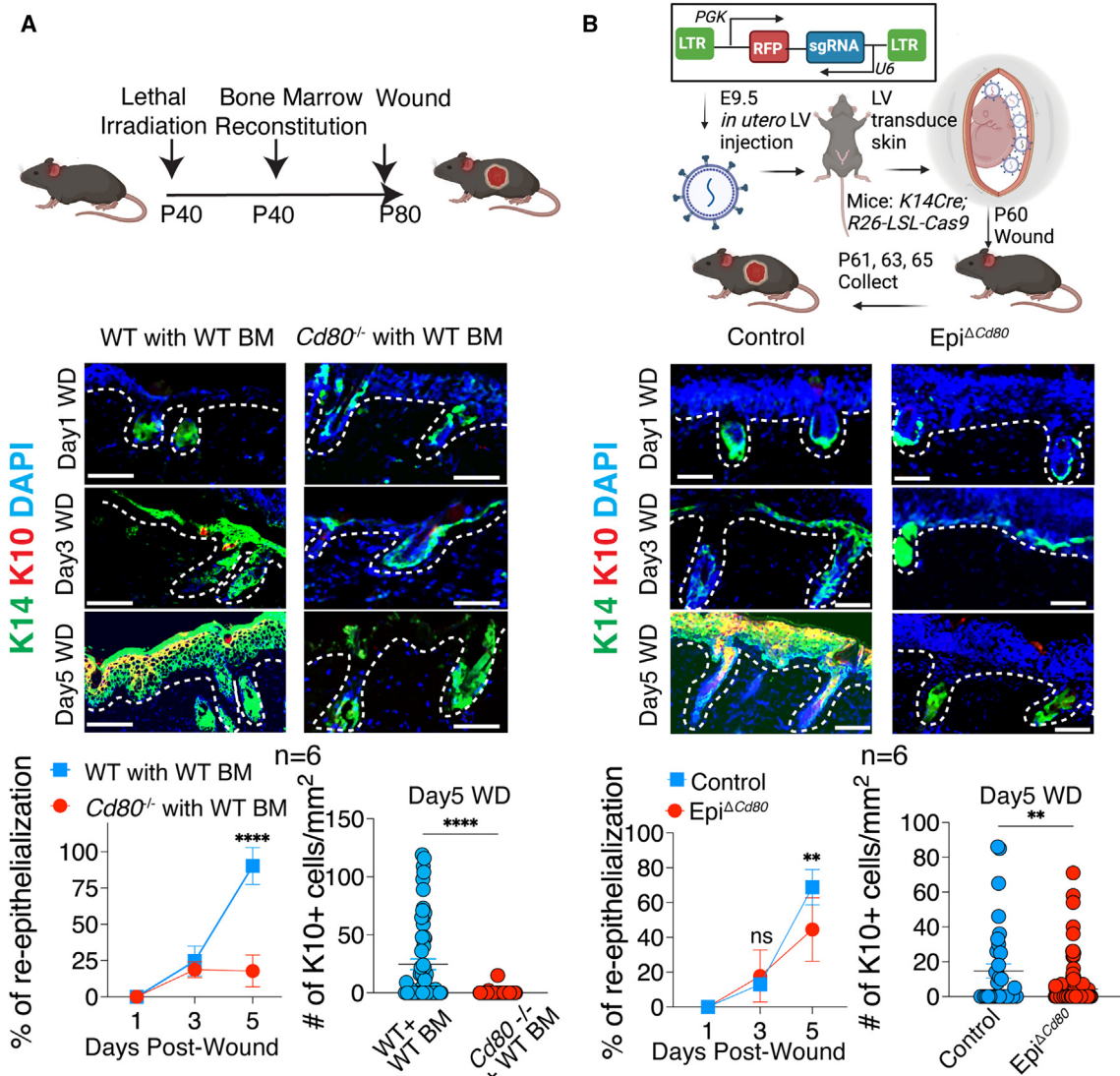


Figure 3. Specific ablation of CD80 in HFSCs results in wound healing delays

(A) Schematic of wounding in irradiated $Cd80^{-/-}$ or WT control mice and reconstituted with WT bone marrow (BM). Shown below are IF images and quantifications of the percentage of wound re-epithelialization ($K14^{+}$) and the number of differentiated suprabasal cells ($K10^{+}$) in the skins at times indicated after partial-thickness wounding.

(B) Schematic is of lentivirus injected into the amniotic sac of E9.5 embryos of *Krt14-Cre; Rosa26-LSL-Cas9* mice to specifically transduce surface epithelial skin progenitors, here with $Cd80$ -targeting sgRNAs ($Epi^{\Delta Cd80}$) or use Cre negative mice as controls. Shown below are IF images and quantifications of the percentage of wound re-epithelialization ($K14^{+}$) and the number of differentiated suprabasal cells ($K10^{+}$) in the skins at times indicated after partial-thickness wounding. Each symbol represents a technical replicate. Results pooled from two independent experiments are shown as mean \pm SEM ($n = 3$ animals for each time point in each experiment). Unpaired t test; ** $p < 0.01$, **** $p < 0.0001$. Scale bars, 100 μ m. See also Figure S2.

With this approach, when we wounded mice that had received *in utero* $Cd80$ sgRNA as described above and were conditionally ablated for $Cd80$ in their skin epithelium ($Epi^{\Delta Cd80}$), pronounced delays were evident in both the re-epithelialization and differentiation phases of the repair process (Figure 3B). Similar to wounds of $Cd80$ null mice reconstituted with a WT hematopoietic system, which closed by day 9, wounds of *Krt14 Cre*-driven $Epi^{\Delta Cd80}$ mice closed by day 7, i.e., approximately 4 and 2 days, respectively, after control mice. The somewhat faster rate seen in $Epi^{\Delta Cd80}$ mice versus our BM reconstituted mice was likely because of a small per-

centage of imperfect gene editing (escapers) within *Krt14 Cre*-driven skin SCs.

Taken together, the consistent and pronounced 2–4-day delay in the re-epithelialization and differentiation process seen when HFSCs entering the wound bed failed to induce CD80 provided compelling evidence that the immune-modulatory capacity of epithelial SCs plays a vital role in cutaneous wound repair. Moreover, since the defect was observed when CD80 induction was missing in HFSCs but still present in immune cells, these data further indicated that CD80 is an intrinsic and essential feature of wound-activated HFSCs.

CD80 in HFSCs orchestrates Treg cell responses at the wound bed to drive re-epithelialization

It was surprising that CD80, typically viewed as a protein exclusive to antigen-presenting immune cells, was found to be both induced in and essential for wound-mobilized epithelial SCs to efficiently heal skin wounds. The importance of epithelial SC-specific CD80 expression was all the more intriguing given that CD80 was only detected in a subset of wound-activated integrin $\alpha 5^+$ migrating HFSCs. Upon antigen presentation by CD80-expressing DCs, CD80 engages its receptor CD28 to provide co-stimulatory signals to T lymphocytes.²⁸ We therefore turned to addressing the tantalizing possibility that HFSC CD80 might function to modulate the immune microenvironment surrounding the epithelial SCs in the wound bed to be conducive for the re-epithelialization process.

At 5 days post-wounding, CD4⁺ T cells were significantly increased in WT but not in Epi ^{$\Delta Cd80$} wounds (Figure 4A). In particular, the Foxp3⁺ Treg cell population, not the Foxp3^{neg} conventional T (Tconv) cells, displayed a striking expansion in WT wounds but not in Epi ^{$\Delta Cd80$} wounds (Figures 4B and 4C). By contrast, no significant differences in Treg cell numbers or other features of the immune landscape were observed between the unwounded, homeostatic skin of Epi ^{$\Delta Cd80$} and control mice (Figures S3A and S3C), indicating that skin SC-induced CD80 is particularly important for the wound repair process.

Treg cells are a group of suppressive immune cells that prevent deleterious autoimmunity and dampen inflammation.^{29,30} Treg cell depletion has been reported to attenuate the closure of skin wounds after injury,^{31,32} and hence we were not surprised to see that upon administering diphtheria toxin (DT), re-epithelialization and differentiation were defective in Foxp3-promoter-driven DT receptor mice (Figure 4D). However, our new data now pointed to the idea that, following injury, wound-mobilized SCs may function critically in mounting the robust Treg cell response necessary to facilitate the re-epithelialization process. Moreover, this powerful attribute appeared to be rooted in their ability to induce the expression of CD80 during wound repair.

To further bolster this conclusion, we constructed BM chimeras, reconstituting either irradiated WT or $Cd80^{-/-}$ mice with the BM from *Foxp3*-GFP reporter mice as a reliable way to visualize the dynamics of Treg cell responses during wound repair. Immunofluorescence and quantifications of the distance between CD3⁺/Foxp3-GFP⁺ Treg cells and K14⁺ SCs in *de novo* regenerating epithelium revealed that, strikingly, Treg cells accumulate just beneath the epithelium in WT wounds (Figures 4E and 4F). Moreover, this Treg cell barrier was lost when HFSCs were targeted for $Cd80$ ablation, underscoring the importance of SC-specific CD80 induction in generating and/or maintaining this protective web.

Taken together, these data underscored the importance of not merely Treg cells but also CD80-expressing epithelial SCs in wound repair. Moreover, our data further unearthed an intricate coordination between Treg cells and CD80-expressing wound-mobilized epithelial SCs in governing the immunomodulatory action required for the re-epithelialization process.

Epithelial SCs prevent Neu accumulation near the wound site

Probing for other changes in the immune response of our wound-induced, epithelial-specific $Cd80$ ablation (Epi ^{$\Delta Cd80$}), we observed significantly more immune cells (CD45⁺) compared with control mice (Figures S3B and S3C). In particular, Neu accumulated at much higher levels, as evidenced by hematoxylin and eosin staining (Figure 5A) and ultrastructural analyses (Figure 5B). The increase of CD11b⁺/Ly6G⁺ Neu in the wounds of Epi ^{$\Delta Cd80$} mice compared with control mice was also confirmed by flow cytometry quantification (Figure 5C). Immunofluorescence microscopy staining of the wounds at 5 days post-wounding further substantiated the persistence of elevated Neu within the wound bed of $Cd80$ null mice at a time when Neu in control wounds had waned concomitant with re-epithelialization (Figure 5D). Interestingly, a recent study reported that Treg cells in the wound are responsible for stopping the Neu accumulation and that loss of Treg cells can cause extensive inflammation induced by Neu.³² Our data here showed that if epithelial SCs cannot induce CD80 following injury, they are incapable of orchestrating the immune cell dynamics needed to suppress inflammation and facilitate re-epithelialization at the wound bed.

HFSCs facilitate the expansion of extrathymic Treg cells in the wound

Treg cells can develop both in the thymus (tTreg cells) and in the peripheral lymphoid tissues (pTreg cells).^{29,30} Therefore, we sought to distinguish whether CD80 molecules presented by HFSCs at the re-epithelialization front act by recruiting more tTreg cells from circulation or, alternatively, by stimulating the expansion of extrathymic pTreg cells induced during wound repair. To do so, we first designed a Treg cell fate-mapping assay in which preexisting Treg cells could be distinguished from the extrathymic pTreg cells induced during wound repair.

To this end, we sought to design a series of BM chimeras to perform lineage tracing. First, as a control experiment, we grafted the lethally irradiated $Cd80$ null and WT mice with congenic marker CD45.1⁺ BMs (Figure S4A). Our data from these mice confirmed that more than 70% of Foxp3⁺ Treg cells in the wound are CD45.1⁺ (Figure S4B), and CD80 deficiency mostly causes reductions in donor-derived CD45.1⁺ Treg cells (Figures S4C and S4D). By contrast, the CD45.1^{neg} tissue-resident Treg cells remaining in the tissue after irradiation were not obviously affected by the absence of CD80 in HFSCs (Figures S4C and S4D).

Based on this premise, we next reconstituted the hematopoietic system of the WT or $Cd80$ null mice by transplanting extracted BM from *Foxp3*-GFP-CreER; *Rosa26-LSL-tdTomato* mice. In these chimeric mice, tamoxifen treatment before wounding induced the expression of the fate-mapping marker, tdTomato, and labeled pre-existing Foxp3⁺GFP⁺ Treg cells with tdTomato (double-positive [DP]). Thus, following tamoxifen exposure and subsequent wounding, those pre-existing Treg cells that entered the skin from the circulation were DP, while those induced after skin injury were marked by GFP alone (single-positive [SP]) (Figure 6A). Interestingly, 5 days after wounding, the percentage and numbers of GFP SP Treg cells increased significantly in WT wounds, but not in the wounds where HFSCs cannot activate CD80 (Figure 6A). These results provided

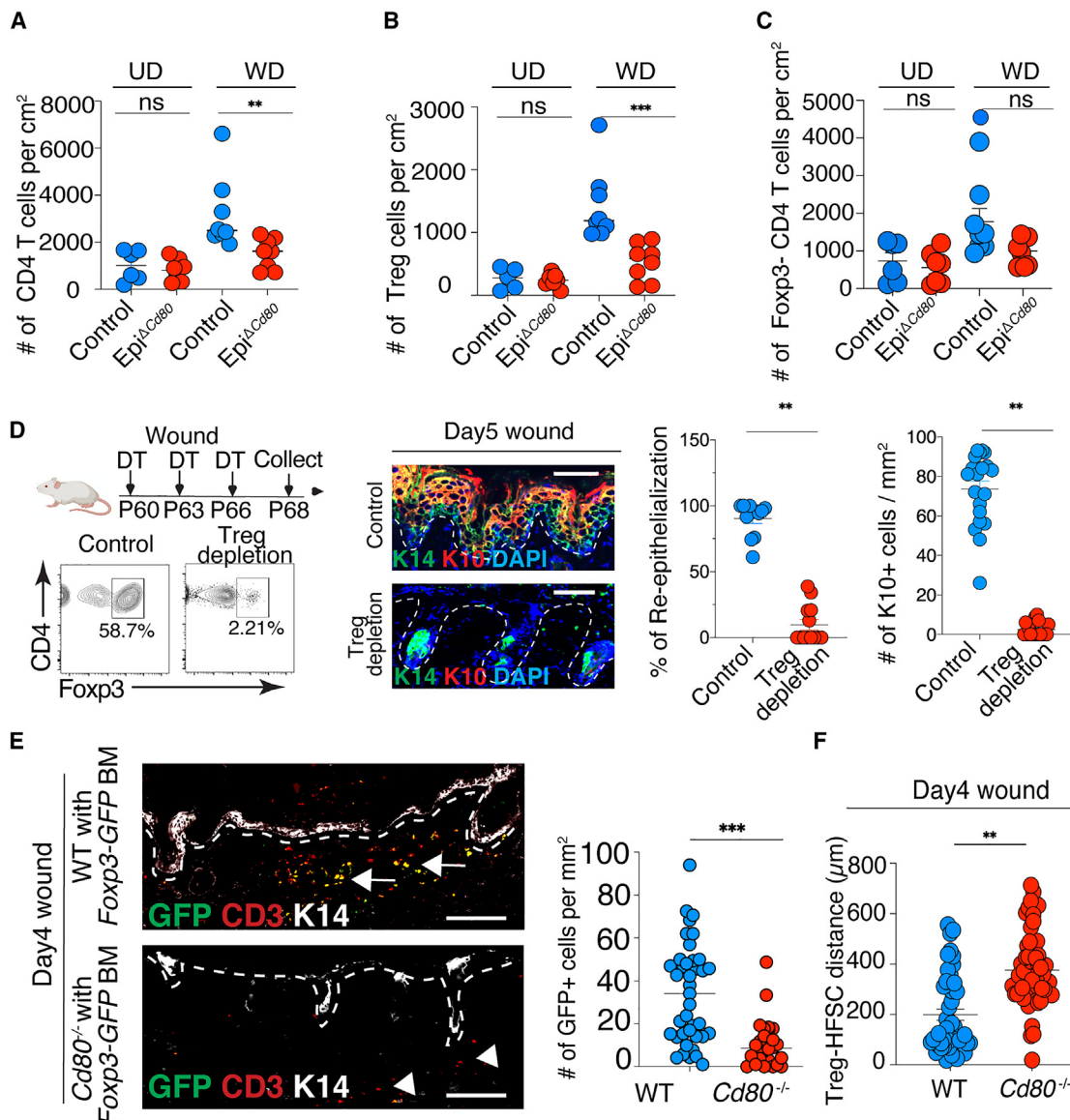


Figure 4. Wound-induced migrating SCs express CD80 to stimulate local Treg cell expansion and create a protective niche around the re-epithelializing tissue

(A–C) Total CD4 T cells (A), Foxp3⁺ Treg cells (B), and Foxp3⁻ Tconv cells (C) are quantified by flow cytometry in unwounded (UD) or wounded (WD) skin at day 5 following injury. $n = 9$ pooled from three independent experiments. Each symbol represents an individual animal. Pooled quantifications from three independent experiments are shown as mean \pm SEM.

(D) Schematic and flow cytometry quantification below show efficient Treg cell depletion. IF and quantification show re-epithelialization (K14⁺) and differentiation (K10⁺) in mice with or without Treg cell depletion.

(E) IF images of total GFP⁺CD3⁺ Treg cells (quantified at right) that infiltrate the skin wounds of WT or *Cd80*^{-/-} mice reconstituted with bone marrow from *Foxp3-GFP* Treg cell reporter mice. Each symbol represents a technical replicate. Representative images and pooled quantifications from two independent experiments are shown as mean \pm SEM.

(F) Quantification of the distance between GFP⁺ Treg cells that enter/expand within the wound bed in (E) from the migrating epithelial SCs. Each symbol represents a technical replicate.

Unpaired t test; * $p < 0.05$, ** $p < 0.01$, *** $p < 0.001$. Scale bars, 100 μm . See also Figure S3.

compelling evidence that the CD80 expressed by wound-mobilized HFSCs is critical for stimulating the expansion of peripherally induced Treg cells after they arrived in the skin.

Extrathymic induction of Treg cells from CD4⁺ T cells depends upon a TGF- β responsive element within the *Foxp3*

enhancer referred to as conserved non-coding sequence 1 (CNS1), but this element is dispensable for the tTreg cell maturation that occurs within the thymus.³³ To further challenge a model in which wound-activated CD80-expressing HFSCs stimulate the local expansion of newly induced pTreg

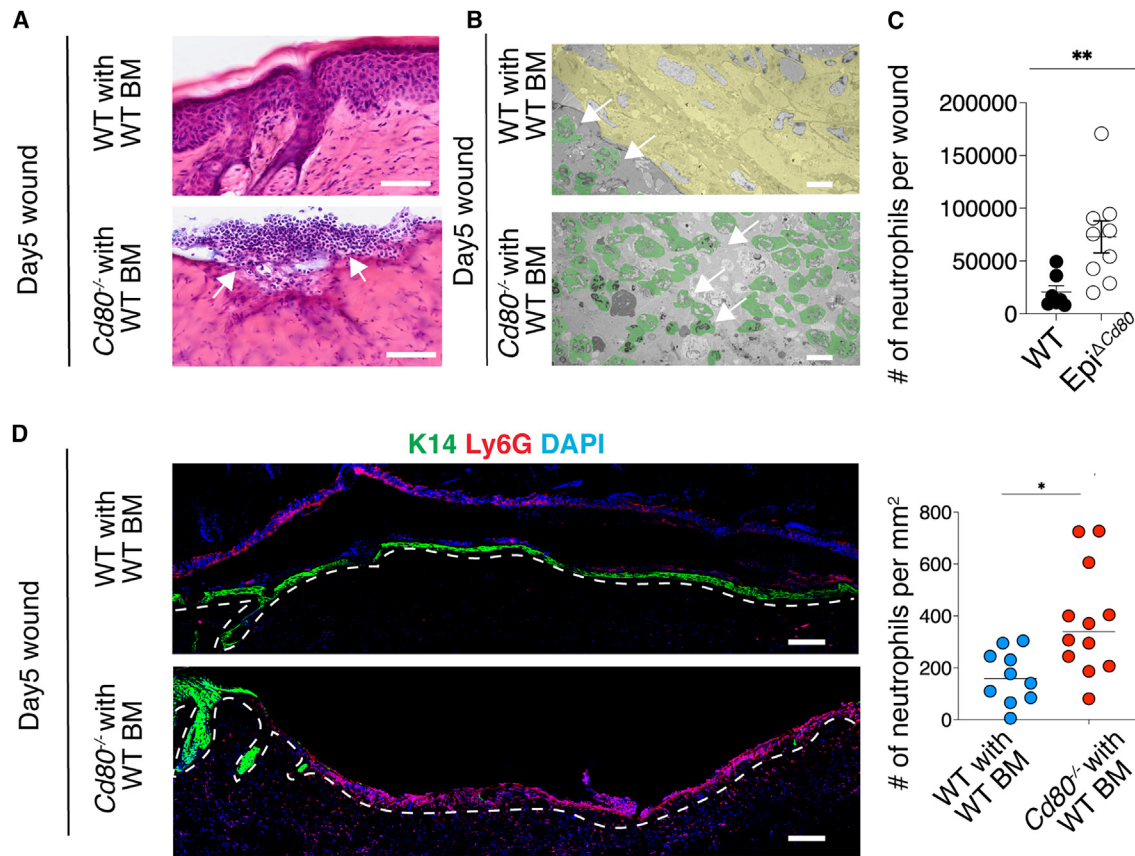


Figure 5. CD80 is important for skin SCs to suppress neutrophil infiltration into the re-epithelializing wound bed

(A) Hematoxylin and eosin staining of the wounded skin from WT or $Cd80^{-/-}$ mice reconstituted with WT bone marrow. Representative images from two independent experiments are shown. Scale bars, 100 μ m.

(B) Ultrastructural images of the wounded skin from WT or $Cd80^{-/-}$ mice reconstituted with WT bone marrow. Arrows point to polymorphonuclear cells. Neutrophils are color-coded in green. The re-epithelialized skin is color-coded in yellow. Representative images from two independent experiments are shown. Scale bars, 10 μ m.

(C) Flow cytometry quantification of the number of Ly6G hi neutrophils within the CD11b $^+$ MHCII low immune population in day 5 wounds on control or Epi Δ Cd80 mice. Each symbol represents an individual animal. Pooled quantifications from three independent experiments are shown as mean \pm SEM.

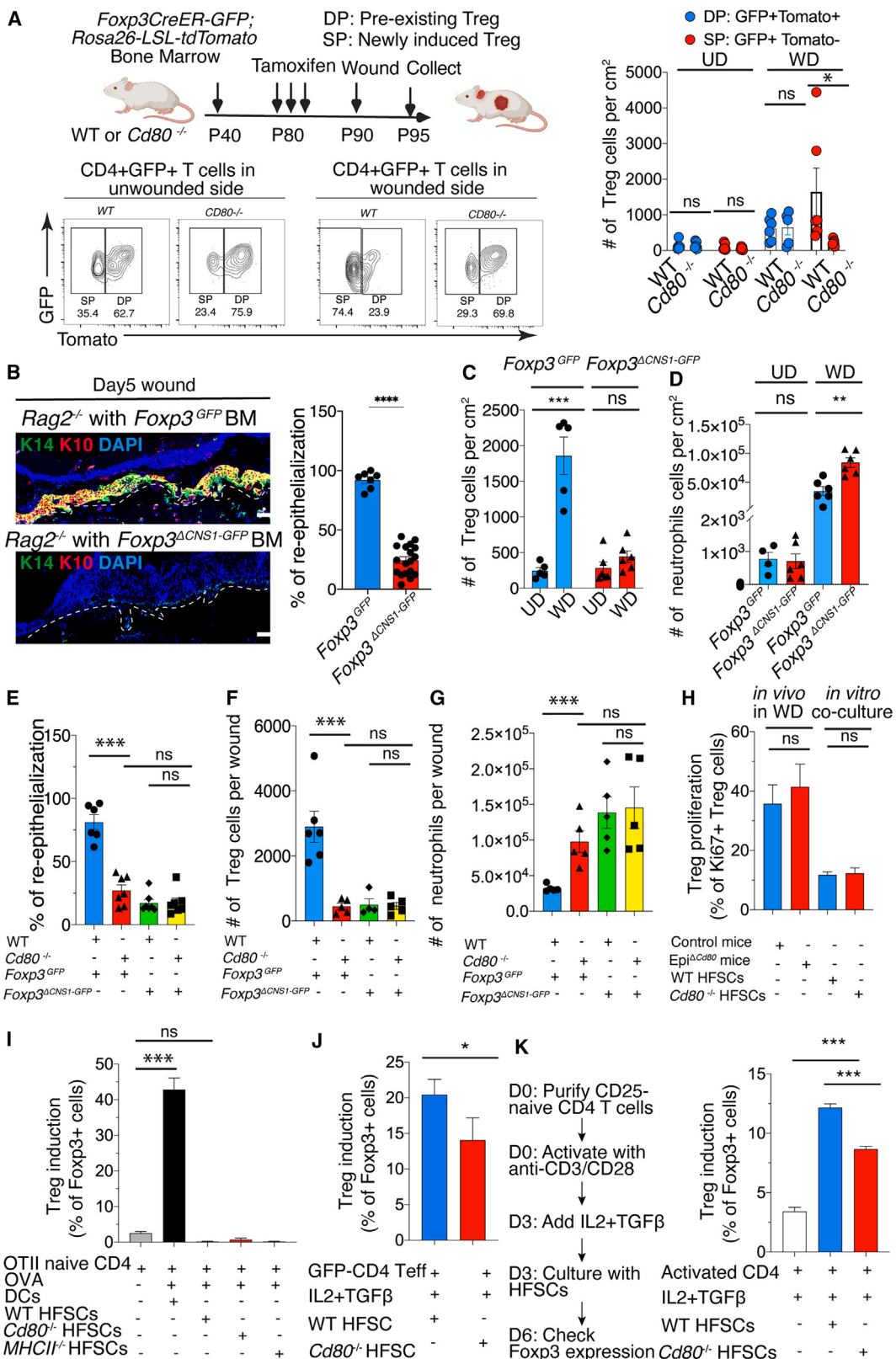
(D) IF images and quantifications of Ly6G $^+$ neutrophils per mm^2 in wounded skin from WT or $Cd80^{-/-}$ mice reconstituted with WT bone marrow. Each symbol represents a technical replicate. Representative images and pooled quantifications from two independent experiments are shown. Scale bars, 100 μ m.

Unpaired t test; * $p < 0.05$, ** $p < 0.01$.

cells, we irradiated B and T cell-deficient $Rag2^{-/-}$ mice and reconstituted them with BM from strain-matched $Foxp3^{GFP}$ ($Foxp3tm2Ayr$) control or $Foxp3^{\Delta CNS1-GFP}$ mice.³³ Upon wounding, the mice reconstituted with $Foxp3^{\Delta CNS1-GFP}$ BM displayed defects in re-epithelialization and differentiation that resembled those of Epi Δ Cd80 mice (Figure 6B). Additionally, immune profiling showed that, in contrast to the wounds of mice reconstituted with $Foxp3^{GFP}$ control BM, these wounds were marked by a paucity of Treg cells (Figure 6C) and failed to dampen Neu infiltration into the wound bed (Figure 6D). Finally, irradiated $Cd80^{-/-}$ mice that had been reconstituted with BM harboring the genomic CNS1 deletion showed a similar degree of Treg cell deficiency following wounding. As expected, reconstitution of irradiated $Cd80^{-/-}$ mice with BM harboring the genomic CNS1 deletion did not result in any additional defects in re-epithelialization, Treg cell induction, and Neu reduction (Figures 6E–6G).

HFSCs trigger Treg cell induction from pre-activated CD4 T cells in a CD80 dependent but MHC-class II-independent manner

So far, our data pointed to the view that extrathymic pTreg cells expand as a consequence of CD80 $^+$ HFSC stimulation and are the main population responsible for protecting HFSCs during wound healing. Next, we sought to dissect the underlying basis of this close interaction between HFSCs and Treg cells. The simplest possibility was that the pTreg cells had originated from the peripheral lymphoid organs, and once recruited into the wound, CD80 on HFSCs provided co-stimulatory signals that enhanced their proliferation. Interestingly, however, among the Treg cells that infiltrated the wounded skin, Ki67 levels were similar between control and Epi Δ Cd80 mice (Figure 6H). This was also the case when we wounded the $Foxp3$ -GFP reporter mice, isolated GFP $^+$ Treg cells from the wound-draining lymph nodes, and co-cultured them with HFSCs purified from either WT or $Cd80^{-/-}$ mice (Figure 6H).



(legend on next page)

In the peripheral lymphoid organs, generation of pTreg cells from naive CD4 T cells is dependent on tolerogenic CD80⁺MHCII⁺ DCs providing antigen presentation and co-stimulation. Given that a subset of HFSCs that migrate into the wound also express both MHCII and CD80, we asked whether HFSCs might be able to directly induce naive CD4 T cells to differentiate into Treg cells. To test this possibility, we isolated naive CD4 T cells from OT II mice and co-cultured them with the HFSCs in the presence of IL-2 and TGF-β. Importantly, the HFSCs were preloaded with either the ovalbumin (OVA) protein or the OVA-derived peptide (323–339), which is recognized by TCRs of OT II mice when presented on MHCII complex. However, no Treg cell induction was seen in these co-cultures (Figure 6I). We also ablated class II MHCs first in the basal skin epithelium using *Krt14-Cre*; MHCII^{flox/flox} mice or specifically in HFSCs using *Sox9CreER*; MHCII^{flox/flox} mice (*Epi*^{ΔMHCII}). Whether we targeted MHCII ablation during embryonic development or just before wounding, we observed no overt phenotypic differences in re-epithelialization, Treg cell induction, or Neu accumulations in both models (Figure S5). From these data, we concluded that although MHCII is expressed by HFSCs, it is dispensable for SC-mediated Treg cell induction and wound repair and, in this way, differed from CD80. Taken together, our MHCII results were in agreement with our co-culture result that HFSCs cannot induce naive CD4 T cells to differentiate into Treg cells.

Most CD4 T cells encountered by HFSCs in the wound bed should have already been activated in the lymph nodes immediately after injury. We therefore turned to the notion that activated T cells might be able to respond to CD80⁺ HFSCs in the wound bed and elevate Foxp3 expression. To test this hypothesis, we isolated *Foxp3-GFP*^{neg}CD62L^{Low}CD44^{Hi} CD4 T cells from the draining lymph nodes of wounded Treg cell reporter mice and co-cultured them with HFSCs isolated from WT or CD80 null mice. Interestingly, compared with the CD80 null HFSCs, WT HFSCs induce higher Foxp3 expression in CD4 T cells (Figure 6J). To further test our hypothesis, we isolated naive CD4 T cells, pre-activated these CD4 T cells with CD3/CD28 antibody, and only exposed these newly activated T cells to TGF-β after they were activated (Figure 6K). Interestingly, when we added WT HFSCs to this culture, the activated CD4 T cells can

re-gain their capacity to respond to TGF-β and maintain Foxp3 expression in a manner dependent upon sustained presence of HFSC CD80 (Figure 6K).

Overall, these results suggest that CD80 presented by wound-activated epithelial SCs can alter the differentiation potential of activated CD4 T cells and trigger TGF-β-sensitive (CNS1) enhancer activity within the *Foxp3* locus. In doing so, the SCs weave a protective Treg cell web that specifically envelopes them at the wound bed until they have repaired the skin's barrier.

HFSCs balance inflammation and immune tolerance during wound repair

Recently, it was observed that Treg cell depletion, followed by mechanical abrasion of the skin, leads to a raging inflammatory Neu response in the wound bed. The increased Neu accumulation in these wounds seemed to be fueled, at least in part, by epithelial cell production of the Neu chemoattractant CXCL5.³² Advancing this knowledge further, we traced the source of epithelial *Cxcl5* to the integrin α5⁺ HFSCs that mark the re-epithelializing wound front (Figure 1C) and that ironically display CD80 to modulate Treg cells (Figure 7A). ATAC-seq of the isolated HFSCs further revealed marked changes in the accessibility of the *Cxcl5* locus following injury (Figure 7B). As shown by qPCR analysis, *Cxcl5* transcripts were rapidly and transiently elevated by >300-fold in HFSCs within a single day after wounding (Figure 7C).

Collectively, our results suggested that paradoxically, wound-activated skin SCs are the major population that induces CXCL5 to stimulate Neu recruitment and inflammation. Interestingly, while *Cxcl5* mRNA levels waned in control animals by day 4 post-wounding, *Cxcl5* remained higher in mice whose HFSCs were ablated for *Cd80* (Figure 7D). Higher levels of *Cxcl5* transcripts were also observed in the wounds of *Rag2* null mice reconstituted with *Foxp3*^{ΔCNS1-GFP} compared with control BM. This was corroborated by RNAscope used to analyze *Cxcl5* levels *in situ*, showing that *Cxcl5* transcripts accumulated mainly in K14⁺ skin epithelial cells that had migrated into the wound bed (Figure 7E). This result suggests that the increased CXCL5 seen in CD80-deficient migratory HFSCs might be triggered by the corresponding paucity of pTreg cells in the wound bed (Figure 7E). These observations further bolstered the conclusion

Figure 6. CD80 expression by migrating epithelial SCs promotes the expansion of extrathymically induced Treg cells during wound healing
(A) Schematic of experimental design and flow cytometry quantification of the frequency and number of preexisting (double positive: Tomato⁺GFP⁺) and newly induced (single positive: GFP⁺Tomato⁻) Treg cells in day 5 wounds ($n = 3$ in each experiment). Representative flow cytometry plots and pooled quantifications from two independent experiments are shown as mean ± SEM.
(B–D) IF images and quantification of re-epithelialization (B), flow cytometry quantifications of the Treg cells (C), and neutrophils (D) in the day 5 wounds from skins of *Rag2*^{−/−} mice that were reconstituted with *Foxp3*^{GFP} control or *Foxp3*^{ΔCNS1-GFP} bone marrow. Scale bars, 100 μm. Representative images and pooled quantifications from two independent experiments are shown as mean ± SEM.
(E–G) Image quantification of re-epithelialization (E) and flow cytometry quantifications of the Treg cells (F) and neutrophils (G) in the day 5 wounds from skins of WT or *Cd80*^{−/−} mice that were reconstituted with *Foxp3*^{GFP} control or *Foxp3*^{ΔCNS1-GFP} bone marrow. Each symbol is an individual animal. Pooled data from two independent experiments are shown as mean ± SEM.
(H) Flow cytometry quantifications of Ki67⁺ Treg cells in day 5 wounds from skins of control or *Epi*^{ΔCd80} mice (*in vivo*) or after co-culturing the GFP⁺ Treg cells with WT or *Cd80*^{−/−} HFSCs for 3 days.
(I–K) Flow cytometry quantification of Foxp3 induction in CD4 T cell after: (I) naive CD4 T cells from OT II mice are co-cultured with WT, *Cd80*^{−/−}, or MHCII^{−/−} HFSCs that are pre-loaded with OVA protein or OVA peptides in the presence of IL-2 and TGF-β; (J) CD4⁺ GFP^{neg} CD44^{Hi} CD62L^{Low} T cells are isolated from wound draining lymph nodes in *Foxp3-GFP* mice and co-cultured with WT or *Cd80*^{−/−} HFSCs in the presence of IL-2 and TGF-β; (K) naive CD4 T cells are activated with anti-CD3/CD28 for 3 days, followed by co-culturing with WT or *Cd80*^{−/−} HFSCs, and TGF-β is only added together with HFSCs. Representative data from one of the three independent experiments are shown as mean ± SEM.
Two-way ANOVA with the Bonferroni correction for (A)–(G), unpaired t test for (H)–(K). *** $p < 0.0001$, ** $p < 0.001$, * $p < 0.01$, $*p < 0.05$. See also Figures S4 and S5.

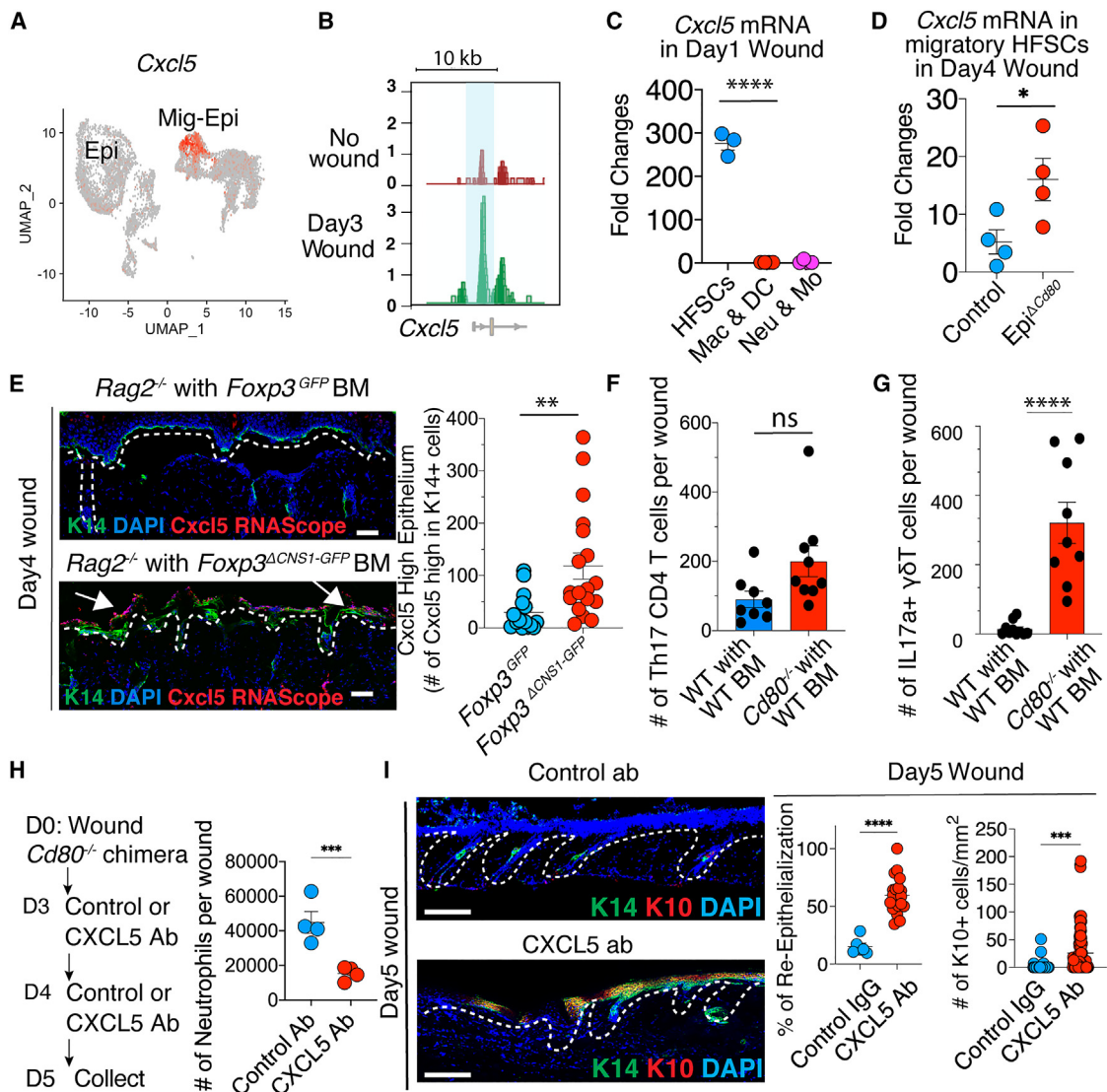


Figure 7. Skin SCs balance inflammation and Treg cell-mediated immune tolerance during wound repair

(A) UMAP plot showing that *Cxcl5* is specifically activated in the integrin $\alpha 5^+$ epithelial SCs (see Figure 1D) that have migrated into the wound.

(B) ATAC-seq peak showing the accessibility status of the *Cxcl5* locus in lineage-traced epithelial SCs sorted from unwounded or day 3 post-wounded Sox9-lineage-traced epithelial SCs.

(C) qPCR quantifications of *Cxcl5* expression in mobilized HFSCs, macrophages (MACs)/dendritic cells (DCs), and neutrophils (Neu)/monocytes (Mo) isolated from day 1 wounds.

(D) qPCR quantifications of *Cxcl5* expression in integrin $\alpha 5^+$ epithelial SCs isolated from day 4 wounds of WT or Epi^{ΔCd80} mice.

(E) Images and quantification of K14⁺ epithelium (green) and RNAScope probing the transcript of *Cxcl5* (red) in wounds from skins of *Rag2*^{-/-} mice reconstituted with *Foxp3*^{GFP} control or *Foxp3*^{ΔCNS1-GFP} bone marrow. Each symbol represents a technical replicate. Representative images and pooled quantification from two independent experiments are shown as mean \pm SEM. Scale bars, 100 μ m.

(F and G) Flow cytometry quantifications of IL-17 production in (F) TCR β^+ CD4 $^+$ T cells or (G) TCR β^- TCR $\gamma\delta^+$ T cells in day 4 wounds from skin of WT or Cd80^{-/-} mice receiving WT bone marrow. Each symbol represents an individual animal. Pooled quantifications from two independent experiments are shown as mean \pm SEM.

(H and I) Schematic, IF images, and quantification showing re-epithelialization process and differentiation after control or CXCL5 Ab treatment of Cd80^{-/-} mice reconstituted with WT bone marrow. Each symbol represents a technical replicate. Representative images and pooled quantifications from one of the two independent experiments are shown as mean \pm SEM.

Unpaired t test, *** p < 0.0001, ** p < 0.001, * p < 0.05. Scale bars, 100 μ m.

that the migratory HFSCs are the orchestrators balancing inflammation and tolerance during the wound repair.

Our findings were intriguing in light of a recent study that suggested that Treg cells reduce Neu accumulation in cutaneous

wounds by blocking IL-17 production in T cells.³² As our wounded Epi^{ΔCd80} mice showed a decrease in Treg cells and increase in Neu, we wondered if IL-17 production might be elevated in these lymphocytes. Although we did not observe

increased IL-17 in CD4 T cells (Figure 7F), we did find that loss of CD80 in HFSCs resulted in enhanced IL-17 production in $\gamma\delta$ T cells (Figure 7G). Our results are consistent with recent reports that $\gamma\delta$ T cells are the main source of IL-17 after tissue injury.^{9,34,35} Together, our results suggest that CD80 presentation by epithelial cells is required to stimulate Treg cells, which in turn may suppress Neu-mediated inflammation in the wound by dampening down $\gamma\delta$ T cell-mediated IL-17 production and keeping CXCL5 secretion by wound-edge epithelial cells in check.

Finally, to test whether persistence of excess Neu accumulation in the wound bed was the root cause of impaired re-epithelialization and differentiation upon CD80 loss within HFSCs, we administered anti-CXCL5 antibody intraperitoneally to *Cd80* null mice on days 2 and 4 post-wounding.³² Notably, this suppressed the Neu influx (Figure 7H) and significantly rescued the re-epithelialization and differentiation defects in these mutant mice (Figure 7I).

Cumulatively, these data placed the epithelial SCs at the center stage of immune modulation and balancing inflammation and tolerance. Our new findings provided compelling evidence that as epithelial SCs are activated and begin migrating into the wound bed, they express CXCL5 to funnel Neu into the wound bed to efficiently guard against infection until a new barrier is formed. By activating CD80, these mobilized SCs also generate a web of surrounding Treg cells, which in turn provides a buffer zone between the Neu and the epithelial SCs to protect them from the collateral damage otherwise inflicted by the inflammatory Neu, which allows re-epithelialization to occur.

DISCUSSION

HFSCs comprise a vital cellular reservoir for regenerating the skin.^{2,36} Under normal skin homeostasis, HFSCs reside in each follicle within a protective niche replete with an inner layer of protective barrier cells that guards against pathogen entry from the HF orifice to the skin's surface. The skin is also subjected to frequent shallow wounds, compromising the skin's surface barrier and mobilizing nearby HFSCs to exit their niches and migrate into the wound bed to participate in epidermal repair. There, they encounter a highly inflammatory environment that is essential to contain pathogen infections.^{2,32,36}

It has long been appreciated that inflammation and epithelial repair are incompatible. The traditional view is that these events happen sequentially, although if true, this would generate a window of vulnerability where inflammation would be curbed and healing incomplete. Here, we show that not only can these two incompatible processes co-exist in harmony during a wound response, but in addition, they do so through a dynamic molecular feature of these tissue SCs. Interestingly, when the skin SCs migrate into the wound bed, they sense the damaged tissue environment and respond by weaving a protective niche of Treg cells around them. By suppressing inflammation locally, the Treg cells shield the skin SCs inside this temporary web, enabling the SCs to repair the wound and restore the skin barrier. Outside these confines, the Neu and MACs can continue clearing debris and guarding against pathogens until the wound is healed. By expanding the local Treg cell population to build a Treg cell barrier

against Neu, the SCs at the migrating front of the wound bed can protect themselves from attack even as they secrete the Neu attractant CXCL5 to clear out invading microbes.

We discovered that to perform these extraordinary feats, wound-mobilized skin epithelial SCs upregulate co-stimulatory cell-surface immunomodulatory proteins like CD80, which until recently was thought to be exclusive to classic antigen-presenting immune cells. We stumbled upon CD80 while searching for how cancer SCs of skin squamous cell carcinomas become resistant to cytotoxic T cell attack. In that study, we showed that CD80 was induced in the cancer SCs in response to the enhanced TGF- β within the tumor microenvironment. There, CD80 acted to dampen the potency of cytotoxic T cells, thereby protecting the cancer SCs against immunotherapy-driven attacks.²⁰

Here, we found that in a different setting, namely the TGF- β -enriched environment of damaged tissue, CD80 was again induced, this time within the normal epithelial SCs that enter the wound bed to repair the injury. In this situation, CD8 T cells were a minimal constituent of the normal and wounded skin (Figure S3). In contrast to the cancerous state, expression of CD80 by the SCs in a wound instead played a crucial role in orchestrating the expansion of newly induced extrathymic pTreg cells (Figure 6). This interaction between HFSCs and T cells appeared to buffer the infiltration and accumulation of pro-inflammatory immune cells, such as Neu, thereby allowing the HFSCs to generate new epidermis and restore the skin barrier. It has long been postulated that adult tissue SCs are vulnerable and need to be protected by immune-privileged niches. Our study finds that adult epithelial SCs are an integral part of the immune-modulatory network in the skin. This represents a significant paradigm shift in our understanding of how SCs can drive immune responses and tissue regeneration.

Although the expansion of pTreg cells has previously been attributed to signals derived from antigen-presenting immune cells, our study refocuses the attention to epithelial SCs, which as we show here can co-opt the canonical immune-modulatory machinery in response to inflammation. For barrier tissues like epidermis, re-epithelialization must begin quickly, as keeping microbes out cannot be accomplished until the skin barrier is restored. However, the concomitant generation of an inflammatory environment poised to fight infections is diametrically opposed to barrier restoration. By involving injury-activated SCs in the conversion of infiltrating effector T cells to pTreg cells, Treg cells can be specified and expanded at the right time and place to form a transient immunosuppressive web to protect the SCs within the wound bed and allow them to repair the barrier.

In closing, the intimate interaction between the wound-activated SCs and their ability to stimulate pTreg cells expansion naturally focuses wound-induced pTreg cells toward creating a local Neu-suppressive, repair-conducive microenvironment at the site of re-epithelialization. This web protects the SCs from the harsh inflammatory surroundings of the broader wound site. This intricate, SC-driven orchestration of immunity during wound repair has significant implications for how we think about pathogenic immune responses.

Limitations of the study

Imaging analysis also highlighted the significant distance between HFSCs and Treg cells in the wound bed. Thus, future

studies should investigate whether HFSCs only briefly or transiently interact with T cells in the wound. Additionally, it has been recently reported that intestinal SCs, EpdSCs, and some other tissue cells express MHCII and that the presence of MHCII can increase cytokine production from tissue-resident CD4 T cells, which, in turn, promotes SC functions under normal homeostatic conditions.^{22,23,37} Here, we learned that during a wound response, when HFSCs migrate out of their natural niche and face the robust inflammation of the wound bed, they also express MHCII. However, during wound repair, MHCII appeared to be dispensable for HFSCs to modulate Treg cells, leaving only the CD80-mediated signal to actively sculpt a temporary protective niche comprised of newly generated Treg cells. That said, it remains possible that MHCII molecules may have other important functions during wound repair, and future studies are necessary to further explore their roles in epithelial SCs.

STAR METHODS

Detailed methods are provided in the online version of this paper and include the following:

- KEY RESOURCES TABLE
- RESOURCE AVAILABILITY
 - Lead contact
 - Materials availability
 - Data and code availability
- EXPERIMENTAL MODEL AND STUDY PARTICIPANTS DETAILS
 - Mice
 - Cell Lines
- METHOD DETAILS
 - *In utero* lentiviral transduction
 - Bone marrow chimera construction
 - Partial thickness wound
 - Flow Cytometry
 - Immunofluorescence and RNA scope staining
 - Electron Microscopy
 - *In vitro* co-culture
 - RNA isolation and sequencing library preparation
 - ATAC-Seq library preparation
 - Next generation sequencing data analysis
 - Statistics
 - Data and Software Availability

SUPPLEMENTAL INFORMATION

Supplemental information can be found online at <https://doi.org/10.1016/j.immuni.2024.04.003>.

ACKNOWLEDGMENTS

We thank L. Woodside and J. Stanisovic in the Miao lab and M. Nikolova, E. Wong, and J. Racelis in the Fuchs' lab for technical assistance; R. Niec, S. Naik, and S. Liu (Fuchs' lab) for discussions; J. Levorse for performing LV injections; and S. Dikiy for help with *Foxp3^{ΔCNS1-GFP}* and control mice. We thank B. Ladd, Semova, S. Han, and S. Tadesse (Flow Cytometry Core at the University of Chicago and Rockefeller University) for conducting FACS; P. Faber and C. Lai (Genomics Core at the University of Chicago or Rockefeller University) for sequencing and raw data processing; and the Animal Resources Center at UChicago and Comparative Bioscience Center at Rockefeller for mouse care. E.F. is a Howard Hughes Medical Investigator. This study was supported by Y.M.'s start-up fund and seed grants from The University of Chicago; grants to Y.M. from NIH (R00CA237859, R01CA285786, and R35GM150610), the V Foundation, the American Association for Cancer Research, and The Cancer Research Foundation; and grants to E.F. from the NIH (R01-AR31737, R01-

AR050452, and R37-AR27883) and the Star Foundation, New York State (C32585GG). C.T. was supported by a HHMI Medical Scholar fellowship. N.I. was the recipient of a National Institute of Arthritis and Musculoskeletal and Skin Diseases National Research Service Award (NRSA; F31AR073110). K.S. was a recipient of a Canadian Institute of Health Research Postdoctoral Fellowship.

AUTHOR CONTRIBUTIONS

Y.M., E.F., J.L., C.T., and A.V. conceptualized the study, designed the experiments, interpreted the data, and wrote the manuscript. J.L., C.T., and A.V. performed most experiments and analyzed data from mouse wounding and immunology assays with the assistance from L.P. N.I. performed ATAC-seq. W.G. and K.S. performed RNA-seq and analyzed next-generation sequencing data. J.G., B.L., and A.G. performed and analyzed cell culture and imaging studies. H.A.P. performed electron microscope analysis. E.A. and A.Y.R. maintained and provided *Foxp3^{ΔCNS1-GFP}* and control mice. All authors provided input on the final manuscript.

DECLARATION OF INTERESTS

E.F. is on the editorial board of some Elsevier Journals (*Cell*, *Cell Stem Cell*, and *Developmental Cell*). A.Y.R. is a member of SAB and has equity in Coherus, RAPT Therapeutics, Sonoma Biotherapeutics, Santa Ana Bio, and Vedanta Biosciences; is an SAB member of Biolnvent and Amgen; and holds a therapeutic Treg cell depletion IP licensed to Takeda.

Received: December 12, 2022

Revised: March 21, 2024

Accepted: April 5, 2024

Published: April 26, 2024

REFERENCES

1. Fuchs, E., and Blau, H.M. (2020). Tissue stem cells: architects of their niches. *Cell Stem Cell* 27, 532–556. <https://doi.org/10.1016/j.stem.2020.09.011>.
2. Gonzales, K.A.U., Polak, L., Matos, I., Tierney, M.T., Gola, A., Wong, E., Infarinato, N.R., Nikolova, M., Luo, S., Liu, S., et al. (2021). Stem cells expand potency and alter tissue fitness by accumulating diverse epigenetic memories. *Science* 374, eabh2444. <https://doi.org/10.1126/science.abh2444>.
3. Naik, S., and Fuchs, E. (2022). Inflammatory memory and tissue adaptation in sickness and in health. *Nature* 607, 249–255. <https://doi.org/10.1038/s41586-022-04919-3>.
4. Naik, S., Larsen, S.B., Gomez, N.C., Alaverdyan, K., Sendoel, A., Yuan, S., Polak, L., Kulukian, A., Chai, S., and Fuchs, E. (2017). Inflammatory memory sensitizes skin epithelial stem cells to tissue damage. *Nature* 550, 475–480. <https://doi.org/10.1038/nature24271>.
5. Hsu, Y.C., and Fuchs, E. (2022). Building and maintaining the skin. *Cold Spring Harb. Perspect. Biol.* 14, a040840. <https://doi.org/10.1101/cshperspect.a040840>.
6. Gonzales, K.A.U., and Fuchs, E. (2017). Skin and its regenerative powers: an alliance between stem cells and their niche. *Dev. Cell* 43, 387–401. <https://doi.org/10.1016/j.devcel.2017.10.001>.
7. Aragona, M., Dekoninck, S., Rulands, S., Lenglez, S., Mascré, G., Simons, B.D., and Blanpain, C. (2017). Defining stem cell dynamics and migration during wound healing in mouse skin epidermis. *Nat. Commun.* 8, 14684. <https://doi.org/10.1038/ncomms14684>.
8. Blanpain, C., Lowry, W.E., Geoghegan, A., Polak, L., and Fuchs, E. (2004). Self-renewal, multipotency, and the existence of two cell populations within an epithelial stem cell niche. *Cell* 118, 635–648. <https://doi.org/10.1016/j.cell.2004.08.012>.
9. Liu, S., Hur, Y.H., Cai, X., Cong, Q., Yang, Y., Xu, C., Bilate, A.M., Gonzales, K.A.U., Parigi, S.M., Cowley, C.J., et al. (2023). A tissue injury sensing and repair pathway distinct from host pathogen defense. *Cell* 186, 2127–2143.e22. <https://doi.org/10.1016/j.cell.2023.03.031>.

10. Lu, C.P., Polak, L., Rocha, A.S., Pasolli, H.A., Chen, S.C., Sharma, N., Blanpain, C., and Fuchs, E. (2012). Identification of stem cell populations in sweat glands and ducts reveals roles in homeostasis and wound repair. *Cell* 150, 136–150. <https://doi.org/10.1016/j.cell.2012.04.045>.
11. Page, M.E., Lombard, P., Ng, F., Göttgens, B., and Jensen, K.B. (2013). The epidermis comprises autonomous compartments maintained by distinct stem cell populations. *Cell Stem Cell* 13, 471–482. <https://doi.org/10.1016/j.stem.2013.07.010>.
12. Taylor, G., Lehrer, M.S., Jensen, P.J., Sun, T.T., and Lavker, R.M. (2000). Involvement of follicular stem cells in forming not only the follicle but also the epidermis. *Cell* 102, 451–461. [https://doi.org/10.1016/s0092-8674\(00\)00050-7](https://doi.org/10.1016/s0092-8674(00)00050-7).
13. Ge, Y., Gomez, N.C., Adam, R.C., Nikolova, M., Yang, H., Verma, A., Lu, C.P., Polak, L., Yuan, S., Elemento, O., and Fuchs, E. (2017). Stem cell lineage infidelity drives wound repair and cancer. *Cell* 169, 636–650.e14. <https://doi.org/10.1016/j.cell.2017.03.042>.
14. Agudo, J. (2021). Immune privilege of skin stem cells: what do we know and what can we learn? *Exp. Dermatol.* 30, 522–528. <https://doi.org/10.1111/exd.14221>.
15. Ichiryu, N., and Fairchild, P.J. (2013). Immune privilege of stem cells. *Methods Mol. Biol.* 1029, 1–16. https://doi.org/10.1007/978-1-62703-478-4_1.
16. Paus, R., Bulfone-Paus, S., and Bertolini, M. (2018). Hair follicle immune privilege revisited: the Key to alopecia areata management. *J. Investig. Dermatol. Symp. Proc.* 19, S12–S17. <https://doi.org/10.1016/j.jisp.2017.10.014>.
17. Paus, R., Ito, N., Takigawa, M., and Ito, T. (2003). The hair follicle and immune privilege. *J. Investig. Dermatol. Symp. Proc.* 8, 188–194. <https://doi.org/10.1046/j.1087-0024.2003.00807.x>.
18. Ali, N., Zirak, B., Rodriguez, R.S., Pauli, M.L., Truong, H.A., Lai, K., Ahn, R., Corbin, K., Lowe, M.M., Scharschmidt, T.C., et al. (2017). Regulatory T cells in skin facilitate epithelial stem cell differentiation. *Cell* 169, 1119–1129.e11. <https://doi.org/10.1016/j.cell.2017.05.002>.
19. Liu, Z., Hu, X., Liang, Y., Yu, J., Li, H., Shokhirev, M.N., and Zheng, Y. (2022). Glucocorticoid signaling and regulatory T cells cooperate to maintain the hair-follicle stem-cell niche. *Nat. Immunol.* 23, 1086–1097. <https://doi.org/10.1038/s41590-022-01244-9>.
20. Miao, Y., Yang, H., Levorse, J., Yuan, S., Polak, L., Sribour, M., Singh, B., Rosenblum, M.D., and Fuchs, E. (2019). Adaptive immune resistance emerges from tumor-initiating stem cells. *Cell* 177, 1172–1186.e14. <https://doi.org/10.1016/j.cell.2019.03.025>.
21. Vagaska, B., New, S.E., Alvarez-Gonzalez, C., D'Acquisto, F., Gomez, S.G., Bulstrode, N.W., Madrigal, A., and Ferretti, P. (2016). MHC-class-II are expressed in a subpopulation of human neural stem cells in vitro in an IFNγ-independent fashion and during development. *Sci. Rep.* 6, 24251. <https://doi.org/10.1038/srep24251>.
22. Biton, M., Haber, A.L., Rogel, N., Burgin, G., Beyaz, S., Schnell, A., Ashenberg, O., Su, C.W., Smillie, C., Shekhar, K., et al. (2018). T helper cell cytokines modulate intestinal stem cell renewal and differentiation. *Cell* 175, 1307–1320.e22. <https://doi.org/10.1016/j.cell.2018.10.008>.
23. Fasolino, M., Schwartz, G.W., Patil, A.R., Mongia, A., Golson, M.L., Wang, Y.J., Morgan, A., Liu, C., Schug, J., Liu, J., et al. (2022). Single-cell multi-omics analysis of human pancreatic islets reveals novel cellular states in type 1 diabetes. *Nat. Metab.* 4, 284–299. <https://doi.org/10.1038/s42255-022-00531-x>.
24. Kambayashi, T., and Laufer, T.M. (2014). Atypical MHC class II-expressing antigen-presenting cells: can anything replace a dendritic cell? *Nat. Rev. Immunol.* 14, 719–730. <https://doi.org/10.1038/nri3754>.
25. Xu, L., Kitani, A., and Strober, W. (2010). Molecular mechanisms regulating TGF-beta-induced Foxp3 expression. *Mucosal Immunol.* 3, 230–238. <https://doi.org/10.1038/mi.2010.7>.
26. Haensel, D., Jin, S., Sun, P., Cinco, R., Dragan, M., Nguyen, Q., Cang, Z., Gong, Y., Vu, R., MacLean, A.L., et al. (2020). Defining epidermal basal cell states during skin homeostasis and wound healing using single-cell transcriptomics. *Cell Rep.* 30, 3932–3947.e6. <https://doi.org/10.1016/j.celrep.2020.02.091>.
27. Beronja, S., Livshits, G., Williams, S., and Fuchs, E. (2010). Rapid functional dissection of genetic networks via tissue-specific transduction and RNAi in mouse embryos. *Nat. Med.* 16, 821–827. <https://doi.org/10.1038/nm.2167>.
28. Carreno, B.M., and Collins, M. (2002). The B7 family of ligands and its receptors: new pathways for costimulation and inhibition of immune responses. *Annu. Rev. Immunol.* 20, 29–53. <https://doi.org/10.1146/annurev.immunol.20.091101.091806>.
29. Josefowicz, S.Z., Lu, L.F., and Rudensky, A.Y. (2012). Regulatory T cells: mechanisms of differentiation and function. *Annu. Rev. Immunol.* 30, 531–564. <https://doi.org/10.1146/annurev.immunol.25.022106.141623>.
30. Sakaguchi, S., Mikami, N., Wing, J.B., Tanaka, A., Ichiyama, K., and Ohkura, N. (2020). Regulatory T cells and human disease. *Annu. Rev. Immunol.* 38, 541–566. <https://doi.org/10.1146/annurev-immunol-042718-041717>.
31. Nosbaum, A., Prevel, N., Truong, H.A., Mehta, P., Ettinger, M., Scharschmidt, T.C., Ali, N.H., Pauli, M.L., Abbas, A.K., and Rosenblum, M.D. (2016). Cutting edge: regulatory T cells facilitate cutaneous wound healing. *J. Immunol.* 196, 2010–2014. <https://doi.org/10.4049/jimmunol.1502139>.
32. Mathur, A.N., Zirak, B., Boothby, I.C., Tan, M., Cohen, J.N., Mauro, T.M., Mehta, P., Lowe, M.M., Abbas, A.K., Ali, N., and Rosenblum, M.D. (2019). Treg-cell control of a CXCL5-IL-17 inflammatory axis promotes hair-follicle-stem-cell differentiation during skin-barrier repair. *Immunity* 50, 655–667.e4. <https://doi.org/10.1016/j.jimmuni.2019.02.013>.
33. Zheng, Y., Josefowicz, S., Chaudhry, A., Peng, X.P., Forbush, K., and Rudensky, A.Y. (2010). Role of conserved non-coding DNA elements in the Foxp3 gene in regulatory T-cell fate. *Nature* 463, 808–812. <https://doi.org/10.1038/nature08750>.
34. Hanna, B.S., Wang, G., Galván-Peña, S., Mann, A.O., Ramirez, R.N., Muñoz-Rojas, A.R., Smith, K., Wan, M., Benoist, C., and Mathis, D. (2023). The gut microbiota promotes distal tissue regeneration via RORγt(+) regulatory T cell emissaries. *Immunity* 56, 829–846.e8. <https://doi.org/10.1016/j.jimmuni.2023.01.033>.
35. Konieczny, P., Xing, Y., Sidhu, I., Subudhi, I., Mansfield, K.P., Hsieh, B., Biancur, D.E., Larsen, S.B., Cammer, M., Li, D., et al. (2022). Interleukin-17 governs hypoxic adaptation of injured epithelium. *Science* 377, eabg9302. <https://doi.org/10.1126/science.abg9302>.
36. Lay, K., Yuan, S., Gur-Cohen, S., Miao, Y., Han, T., Naik, S., Pasolli, H.A., Larsen, S.B., and Fuchs, E. (2018). Stem cells repurpose proliferation to contain a breach in their niche barrier. *eLife* 7, e41661. <https://doi.org/10.7554/eLife.41661>.
37. Tamoutounour, S., Han, S.J., Deckers, J., Constantinides, M.G., Hurabielle, C., Harrison, O.J., Bouladoux, N., Linehan, J.L., Link, V.M., Vujkovic-Cvijin, I., et al. (2019). Keratinocyte-intrinsic MHCII expression controls microbiota-induced Th1 cell responses. *Proc. Natl. Acad. Sci. USA* 116, 23643–23652. <https://doi.org/10.1073/pnas.1912432116>.
38. Martin, M. (2011). Cutadapt removes adapter sequences from high-throughput sequencing reads. *EMBnet J.* 17, 10–12. <https://doi.org/10.14806/ej.17.1.200>.
39. Bray, N.L., Pimentel, H., Melsted, P., and Pachter, L. (2016). Near-optimal probabilistic RNA-seq quantification. *Nat. Biotechnol.* 34, 525–527. <https://doi.org/10.1038/nbt.3519>.
40. Love, M.I., Huber, W., and Anders, S. (2014). Moderated estimation of fold change and dispersion for RNA-seq data with DESeq2. *Genome Biol.* 15, 550. <https://doi.org/10.1186/s13059-014-0550-8>.
41. Yu, G., Wang, L.G., Han, Y., and He, Q.Y. (2012). clusterProfiler: an R package for comparing biological themes among gene clusters. *Omics* 16, 284–287. <https://doi.org/10.1089/omi.2011.0118>.
42. Langmead, B., and Salzberg, S.L. (2012). Fast gapped-read alignment with Bowtie 2. *Nat. Methods* 9, 357–359. <https://doi.org/10.1038/nmeth.1923>.

43. Ramírez, F., Dündar, F., Diehl, S., Grüning, B.A., and Manke, T. (2014). deepTools: a flexible platform for exploring deep-sequencing data. *Nucleic Acids Res.* **42**, W187–W191. <https://doi.org/10.1093/nar/gku365>.
44. Hahne, F., and Ivanek, R. (2016). Visualizing genomic data using Gviz and bioconductor. *Methods Mol. Biol.* **1418**, 335–351. https://doi.org/10.1007/978-1-4939-3578-9_16.
45. Zhang, Y., Liu, T., Meyer, C.A., Eeckhoute, J., Johnson, D.S., Bernstein, B.E., Nusbaum, C., Myers, R.M., Brown, M., Li, W., and Liu, X.S. (2008). Model-based analysis of ChIP-Seq (MACS). *Genome Biol.* **9**, R137. <https://doi.org/10.1186/gb-2008-9-9-r137>.
46. Quinlan, A.R., and Hall, I.M. (2010). BEDTools: a flexible suite of utilities for comparing genomic features. *Bioinformatics* **26**, 841–842. <https://doi.org/10.1093/bioinformatics/btq033>.
47. Liao, Y., Smyth, G.K., and Shi, W. (2014). featureCounts: an efficient general purpose program for assigning sequence reads to genomic features. *Bioinformatics* **30**, 923–930. <https://doi.org/10.1093/bioinformatics/btt656>.
48. Hao, Y., Hao, S., Andersen-Nissen, E., Mauck, W.M., 3rd, Zheng, S., Butler, A., Lee, M.J., Wilk, A.J., Darby, C., Zager, M., et al. (2021). Integrated analysis of multimodal single-cell data. *Cell* **184**, 3573–3587.e29. <https://doi.org/10.1093/bioinformatics/btt656>.
49. Buenrostro, J.D., Giresi, P.G., Zaba, L.C., Chang, H.Y., and Greenleaf, W.J. (2013). Transposition of native chromatin for fast and sensitive epigenomic profiling of open chromatin, DNA-binding proteins and nucleosome position. *Nat. Methods* **10**, 1213–1218. <https://doi.org/10.1093/bioinformatics/btt656>.

STAR★METHODS

KEY RESOURCES TABLE

| REAGENT or RESOURCE | SOURCE | IDENTIFIER |
|---|-----------|-------------------------------|
| Antibodies | | |
| APC anti-mouse CD4, rat monoclonal (clone GK1.5) | Biolegend | Cat# 100412; RRID: AB_312697 |
| PE/Cy7 anti-mouse CD4, rat monoclonal (clone GK1.5) | Biolegend | Cat# 100422; RRID: AB_312707 |
| APC/Cy7 anti-mouse CD8b, rat monoclonal (clone YTS156.7.7) | Biolegend | Cat# 126620; RRID: AB_2563951 |
| AF700 anti-mouse CD45, rat monoclonal (clone 30-F11) | Biolegend | Cat# 103128; RRID: AB_493715 |
| APC/Cy7 anti-mouse CD45, rat monoclonal (clone 30-F11) | Biolegend | Cat# 103116; RRID: AB_312981 |
| PE anti-mouse CD45, rat monoclonal (clone 30-F11) | Biolegend | Cat# 103106; RRID: AB_312971 |
| FITC anti-mouse CD45, rat monoclonal (clone 30-F11) | Biolegend | Cat# 103108; RRID: AB_312973 |
| APC/Cy7 anti-mouse CD44, rat monoclonal (clone IM7) | Biolegend | Cat# 103028; RRID: AB_830785 |
| BV711 anti-mouse CD62L, rat monoclonal (clone MEL-14) | Biolegend | Cat# 104445; RRID: AB_2564215 |
| PE anti-mouse CD45.1, mouse monoclonal (clone A20) | Biolegend | Cat# 110707; RRID: AB_313496 |
| PE/Cy7 anti-mouse CD45.1, mouse monoclonal (clone A20) | Biolegend | Cat# 110730; RRID: AB_1134168 |
| APC/Cy7 anti-mouse CD45.2, mouse monoclonal (clone 104) | Biolegend | Cat# 109824; RRID: AB_830789 |
| Pacific Blue anti-mouse CD11b, rat monoclonal (clone M1/70) | Biolegend | Cat# 101224; RRID: AB_755986 |
| PerCP/Cy5.5 anti-mouse CD11b, rat monoclonal (clone M1/70) | Biolegend | Cat# 101228; RRID: AB_893232 |
| PE/Cy7 anti-mouse CD11c, armenian hamster monoclonal (clone N418) | Biolegend | Cat# 117318; RRID: AB_493568 |
| APC anti-mouse CD80, Armenian hamster monoclonal (clone 16-10A1) | Biolegend | Cat# 104714; RRID: AB_313135 |
| AF700 anti-mouse I-A/I-E, rat monoclonal (clone M5/114.15.2) | Biolegend | Cat# 107622; RRID: AB_493727 |
| PE/Cy7 anti-mouse integrin α 5, rat monoclonal (clone 5H10-27 (MFR5)) | Biolegend | Cat# 103816; RRID: AB_2734165 |
| BV711 anti-mouse TCR β Chain, armenian hamster monoclonal (clone H57-597) | Biolegend | Cat# 109243; RRID: AB_2629564 |
| PE anti-mouse TCR γ/δ , armenian hamster monoclonal (clone GL3) | Biolegend | Cat# 118108; RRID: AB_313832 |
| PerCP/Cy5.5 anti-mouse Ki67, rat monoclonal (clone 16A8) | Biolegend | Cat# 652424; RRID: AB_2629531 |
| PE anti-mouse IL-2, rat monoclonal (clone JES6-5H4) | Biolegend | Cat# 503808; RRID: AB_315302 |
| PerCP/Cy5.5 anti-mouse IL17A, rat monoclonal (clone TC11-18H10.1) | Biolegend | Cat# 506920; RRID: AB_961384 |
| FITC anti-mouse IFN- γ , rat monoclonal (clone XMG1.2) | Biolegend | Cat# 505806; RRID: AB_315400 |

(Continued on next page)

Continued

| REAGENT or RESOURCE | SOURCE | IDENTIFIER |
|--|--|------------------------------------|
| FITC anti-mouse Ly-6C, rat monoclonal (clone HK1.4) | Biolegend | Cat# 128006; RRID: AB_1186135 |
| PerCP/Cy5.5 anti-mouse Ly-6C, rat monoclonal (clone HK1.4) | Biolegend | Cat# 128011; RRID: AB_1659242 |
| PE anti-mouse Ly-6G, rat monoclonal (clone 1A8) | Biolegend | Cat# 127608; RRID: AB_1186099 |
| BV711 anti-mouse CD64, mouse monoclonal (clone X54-5/7.1) | Biolegend | Cat# 139311; RRID: AB_2563846 |
| APC anti-mouse Foxp3, rat monoclonal (clone FJK-16s) | ThermoFisher Scientific | Cat# 17-1577-82; RRID: AB_469457 |
| Biotin conjugated anti-CD11b, rat monoclonal (clone M1/70) | Biolegend | Cat# 101204; RRID: AB_312787 |
| Biotin conjugated anti-CD45, rat monoclonal (clone 30-F11) | Biolegend | Cat# 103104; RRID: AB_312969 |
| Biotin conjugated anti-CD31, rat monoclonal (clone MEC13.3) | Biolegend | Cat# 102504; RRID: AB_312911 |
| Biotin conjugated anti-CD117, rat monoclonal (clone 2B8) | Biolegend | Cat# 105804; RRID: AB_313213 |
| Biotin conjugated anti-CD140a, rat monoclonal (clone APA5) | Biolegend | Cat# 135910; RRID: AB_2043974 |
| APC armenian Hamster IgG Isotype Control (clone: HTK888) | Biolegend | Cat# 400911; RRID: AB_2905474 |
| AF700 rat IgG2b κ Isotype Control (clone: RTK4530) | Biolegend | Cat# 400628; RRID: AB_493783 |
| Purified anti-mouse CD3, rat monoclonal (clone 17A2) | Biolegend | Cat# 100202; RRID: AB_312659 |
| Anti-GFP, rabbit polyclonal | Abcam | Cat# ab290; RRID: AB_2313768 |
| Purified anti-Keratin 14, chicken polyclonal (clone Poly9060) | Biolegend | Cat# 906004; RRID: AB_2616962 |
| Purified anti-Keratin 10, rabbit polyclonal (clone Poly19054) | Biolegend | Cat# 905404; RRID: AB_2616955 |
| Purified anti-integrin α5, rat monoclonal (clone 5H10-27 (MFR5)) | BD Biosciences | Cat# 553319; RRID: AB_394779 |
| Purified anti-Ly6G, rat monoclonal (clone 1A8) | Biolegend | Cat# 127602; RRID: AB_1089180 |
| Anti-mouse CD80, goat polyclonal | R&D systems | Cat# AF740, RRID: AB_2075997 |
| AF488 anti-rabbit IgG, donkey polyclonal | Jackson ImmunoResearch Laboratories | Cat# 711-545-152; RRID: AB_2313584 |
| AF488 anti-chicken IgG, donkey polyclonal | Jackson ImmunoResearch Laboratories | Cat# 703-545-155; RRID: AB_2340375 |
| AF488 anti-goat IgG, donkey polyclonal | Jackson ImmunoResearch Laboratories | Cat# 705-545-147; RRID: AB_2336933 |
| AF647 anti-rabbit IgG, donkey polyclonal | Jackson ImmunoResearch Laboratories | Cat# 711-605-152; RRID: AB_2492288 |
| AF647 anti-chicken IgG, donkey polyclonal | Jackson ImmunoResearch Laboratories | Cat# 703-605-155; RRID: AB_2340379 |
| RRX anti-rat IgG, donkey polyclonal | Jackson ImmunoResearch Laboratories | Cat# 712-295-150; RRID: AB_2340675 |
| CD3e monoclonal antibody (clone 145-2C11) | ThermoFisher Scientific | Cat# 14-0031-82; RRID: AB_467049 |
| CD28 monoclonal antibody (clone 37.51) | ThermoFisher Scientific | Cat# 16-0281-82; RRID: AB_468921 |
| Mouse CXCL5 antibody, rat monoclonal (clone 61905) | R&D Systems | Cat# MAB433; RRID: AB_2086587 |

(Continued on next page)

Continued

| REAGENT or RESOURCE | SOURCE | IDENTIFIER |
|---|------------------------------|-----------------|
| Chemicals, peptides, and recombinant proteins | | |
| Tamoxifen | Sigma-Aldrich | Cat# T5648 |
| Diphtheria toxin | Sigma-Aldrich | Cat# D0654 |
| TRIzol | ThermoFisher Scientific | Cat# 15596026 |
| Liberase | Sigma-Aldrich | Cat# 5401020001 |
| Deoxyribonuclease I from bovine pancreas | Sigma-Aldrich | Cat# D4263 |
| Zombie Aqua viability dye | Biolegend | Cat# 423101 |
| Cell stimulation cocktail | ThermoFisher Scientific | Cat# 00-4970-03 |
| Brefeldin A | ThermoFisher Scientific | Cat# 00-4506-51 |
| 2-Mercaptoethanol | ThermoFisher Scientific | Cat# 21985-023 |
| HEPES buffer | Corning | Cat# 25-060-C1 |
| Penicillin-Streptomycin | ThermoFisher Scientific | Cat# 15140122 |
| MEM | ThermoFisher Scientific | Cat# 11140-050 |
| Sodium pyruvate | Corning | Cat# 25-000-C1 |
| Gentamicin | ThermoFisher Scientific | Cat# 15710-064 |
| Mitomycin C | Fisher Bioreagents | Cat# BP25312 |
| OVA 323-339 | InvivoGen | Cat# vac-isq |
| DQ Ovalbumin | ThermoFisher Scientific | Cat# D12053 |
| Recombinant Mouse IL-2 | R&D Systems | Cat# 402-ML-020 |
| Mouse TGF β | Cell Signaling Technology | Cat# 5231LF |
| Critical commercial assays | | |
| MojoSort mouse CD4 naïve T cell isolation kit | Biolegend | Cat# 480040 |
| Foxp3/Transcriptional factor staining buffer set | ThermoFisher Scientific | Cat# 00-5521-00 |
| RNAscope Multiplex Fluorescent Reagent Kit v2 | Advanced Cell Diagnostics | Cat# 323100 |
| RNAscope Probe-Mm-Cxcl5-C1 | Advanced Cell Diagnostics | Cat# 467441 |
| Direct-zol RNA Miniprep Kit | Zymo Research | Cat# 11-331 |
| NEBNext Single Cell/Low input RNA library prep kit for Illumina | New England Biolabs | Cat# E6420S |
| Illumina Tagment DNA Enzyme and Buffer kits | Illumina | Cat# 15027866 |
| MiniElute PCR Purification Kit | Qiagen | Cat# 28004 |
| Deposited data | | |
| RNA-sequencing data | This paper | GEO: GSE220241 |
| ATAC-sequencing data | This paper | GEO: GSE220241 |
| Single cell RNA-sequencing data | Haensel et al. ²⁶ | GEO: GSE142471 |
| Experimental models: Organisms/strains | | |
| Mouse: K14CreER | Fuchs lab | N/A |
| Mouse: K14cre | Fuchs lab | N/A |
| Mouse: Sox9CreER | Fuchs lab | N/A |
| Mouse: Foxp3 ^{ΔCNS1-GFP} | Rudensky lab | N/A |
| Mouse: Foxp3tm2Ayr | Rudensky lab | N/A |
| Mouse: C57BL/6J | The Jackson Laboratory | Cat# 000664 |
| Mouse: B6;129S6-Gt(ROSA)26Sortm9 (CAG-tdTomato)Hze/J | The Jackson Laboratory | Cat# 007905 |
| Mouse: B6.129S4-Cd80tm1Shr/J | The Jackson Laboratory | Cat# 003611 |
| Mouse: B6;129-Gt(ROSA) 26Sortm1 (CAG-cas9*, -EGFP)Fezh/J | The Jackson Laboratory | Cat# 248857 |
| Mouse: B6.129(Cg)-FOXP3tm3 (DTR/GFP)Ayr/J | The Jackson Laboratory | Cat# 016958 |
| Mouse: Foxp3CreER-GFP | The Jackson Laboratory | Cat# 016961 |
| Mouse: B6(Cf)-Rag2tm1.1Gn/J | The Jackson Laboratory | Cat# 008449 |

(Continued on next page)

Continued

| REAGENT or RESOURCE | SOURCE | IDENTIFIER |
|---|-------------------------------------|---|
| Mouse: B6.Cg-Tg(TcrαTcrβ)425Cbn/J | The Jackson Laboratory | Cat# 004194 |
| Mouse: B6.SJL-Ptprca Pepcb/Boyd | The Jackson Laboratory | Cat# 002014 |
| Mouse: B6.129X1-H2-Ab1 tm1Koni/J | The Jackson Laboratory | Cat# 013181 |
| Mouse: B6.129S2-H2dlAb1-Ea/J | The Jackson Laboratory | Cat# 003584 |
| Oligonucleotides | | |
| Mouse Cd80 sgRNA1: CATCAATACGACAATTCCCC | Miao et al. ²⁰ | N/A |
| Mouse Cd80 sgRNA2: CGTGTAGAGGACTTCACCT | Miao et al. ²⁰ | N/A |
| Recombinant DNA | | |
| pLKO-H2BGFP-CD80 sgRNA | Miao et al. ²⁰ | N/A |
| Software and algorithms | | |
| Fiji (Image J) | Fiji (Image J) | https://fiji.sc/ |
| FlowJo | FlowJo | https://www.flowjo.com |
| Biorender | Biorender | www.biorender.com |
| Cutadapt (v3.2) | Martin ³⁸ | https://cutadapt.readthedocs.io/en/v3.4/ |
| Pseudo-aligner Kallisto (v0.44.0) | Bray et al. ³⁹ | https://github.com/pachterlab/kallisto |
| DESeq2 R package (v1.30.0) | Love et al. ⁴⁰ | https://bioconductor.org/packages/release/bioc/html/DESeq2.html |
| clusterProfiler package | Yu et al. ⁴¹ | https://guangchuangyu.github.io/software/clusterProfiler/ |
| MSigDB (Molecular signature database, v7.4) | Broad Institute | https://www.gsea-msigdb.org/gsea/msigdb |
| Bowtie2 (v2.3.4.3) | Langmead and Salzberg ⁴² | http://bowtie-bio.sourceforge.net/owtie2/index.shtml |
| Picard (v2.18.7) | Broad Institute | http://github.com/broadinstitute/picard/releases/tag/2.7.1 |
| DeepTools | Ramirez et al. ⁴³ | https://pypi.org/project/deepTools/ |
| Gviz package | Hahne and Ivanek ⁴⁴ | https://github.com/ivanek/Gviz |
| MACS2 (v2.2.7.1) | Zhang et al. ⁴⁵ | https://pypi.org/project/MACS2/ |
| Bedtools (v2.30.0) | Quinlan and Hall ⁴⁶ | https://bedtools.readthedocs.io/en/latest/ |
| FeatureCounts (v1.5.3) | Liao et al. ⁴⁷ | https://subread.sourceforge.net |
| Seurat (v.4.1.0) | Hao et al. ⁴⁸ | https://github.com/satijalab/seurat |
| R | R Project | https://www.r-project.org/ |
| RStudio | Posit | https://posit.co/download/rstudio-desktop/ |
| Other | | |
| BD FACSaria II Cell Sorter | BD Biosciences | N/A |
| BD LSR II Analyzer | BD Biosciences | N/A |
| BD LSR-Fortessa analyzer | BD Biosciences | N/A |
| Axio Observer Z1 | Zeiss | N/A |
| Leica Stellaris 8 Confocal microscope | Leica | N/A |

RESOURCE AVAILABILITY

Lead contact

Further information and requests for reagents and resources should be directed to the lead contact, Yuxuan Miao (miaoy@uchicago.edu)

Materials availability

This study did not generate unique new reagents.

Data and code availability

- Bulk RNA-seq and ATAC-seq data have been deposited at GEO and are publicly available as of the date of publication. Accession numbers are listed in the [key resources table](#).

- Microscopy data and flow cytometry data reported in this paper will be shared by the [lead contact](#) upon request.
- This paper does not report original code and any additional information or data in this paper will be available from the [lead contact](#) upon request.

EXPERIMENTAL MODEL AND STUDY PARTICIPANTS DETAILS

Mice

Sox9CreER, K14CreER and K14Cre (Fuchs Lab) mice have been previously described and were backcrossed to C57/BL6J background for ten generations. *Foxp3*^{GFP}(*Foxp3tm2Ayr*) and *Foxp3*^{ΔCNS1-GFP} mice were obtained from the Rudensky Lab at Memorial Sloan Kettering Cancer Center. Wild-type C57BL/6J, B6;129S6-Gt(ROSA)^{26Sortm9(CAG-tdTomato)Hze}/J (*R26-LSL-tdTomato*), B6;129S4-Cd80^{tm1Shr}/J (*CD80*^{-/-}), B6;129-Gt(ROSA) 26Sor^{tm1(CAG-cas9*,-EGFP)Fezh}/J (*R26-LSL-Cas9*), B6.129(Cg)-*FOXP3*^{tm3(DTR/GFP)Ayr}/J (*Foxp3-DTR*), *FOXP3*^{tm9(EGFP/creERT2)Ayr}/J (*Foxp3-CreER-GFP*), B6(Cf)-*Rag2*^{tm1.1Gn}/J (*RAG2*^{-/-}), B6.SJL-Ptprc^a Pepc^b/Boyd (*CD45.1*), B6.Cg-Tg(TcraTcrb)425Cbn/J (OTII), MHCII^{f/f} (*B6.129X1-H2-Ab1*^{tm1Koni}/J) and MHCII- (*B6.129S2-H2dlAb1-Ea*/J) mice were obtained from The Jackson Laboratory. Treg cells were depleted in *Foxp3-DTR* mice using a modified protocol.²⁰ Briefly, diphtheria toxin (DT, Sigma-Aldrich) was diluted to 2.5 µg/ml, and 200 µl (0.5 µg) was injected intraperitoneally (i.p.) into WT or *Foxp3-DTR* mice at Day -3, 0 and 3. On day 0, mice were wounded. Neutrophils were depleted via i.p. injection with 50 µg CXCL5 monoclonal neutralizing antibody (R&D systems; mAb 433) at days 3 and 4 post-wounding. To treat mice with tamoxifen, a daily i.p. injection of 100 µg for three consecutive days was performed. All mice were maintained in an Association for Assessment and Accreditation of Laboratory Animal Care (AAALAC)-an accredited animal facility. Procedures were performed using IACUC-approved protocols that adhere to NIH standards. The animals were maintained and bred under specific-pathogen free conditions at the University of Chicago and the Comparative Bioscience Center at Rockefeller University. All the procedures follow the Guide of the Care and Use of Laboratory Animals.

Cell Lines

293FT cells were used for packaging lentivirus and were cultured in Dulbecco's modified eagle medium (DMEM) with 10% FBS, 100 units/mL streptomycin/penicillin, 2 mM glutamine and 1 mM sodium pyruvate.

METHOD DETAILS

In utero lentiviral transduction

Cd80 was specifically edited in the skin of *K14Cre; Rosa26-LSL-Cas9* mice via the ultrasound-guided *in utero* injection of the lentivirus carrying *Cd80* sgRNA and PGK-H2B-RFP reporter. Briefly, pregnant females will be anesthetized using isoflurane gas, and placed onto a heated platform, the female's abdomen will be cleaned of hair using Nair (a common hair removal product for humans, and commonly used on mice to remove hair), and a ventral midline abdominal incision will be made to expose a small part of the uterine horn; a 10cm tissue culture dish, with a hole in the center, will be placed over the incision, and the exposed part of the uterine horn will be gently pulled into the dish, through a slit in the membrane covering the hole; the dish will be filled with PBS to prevent dehydration of the exposed tissue and embryo; the ultrasound transducer will be placed over the embryo and upon identification of the amniotic cavity, a guided microinjection glass capillary loaded with the lentivirus (10⁹ CFU), will be inserted into the amniotic cavity, and the lentivirus injected into the amniotic fluid at a volume of 1 µl to transduce the skin progenitors; four to six embryos will be injected on each side of the uterine horn, and the incision will be closed with catgut suture and wound clips. The pregnant female will be allowed to recover and give birth to lentivirus-transduced pups.²⁷ Once the virus is integrated (~24 hours post-infection), the DNA carried by the lentivirus is stably propagated to the progeny of the epithelial progenitors.²⁷

Bone marrow chimera construction

Recipient mice were lethally irradiated (900 rads), which ensures the depletion of endogenous hematopoietic stem cells. Radiation was delivered in two equal doses (450 rads each), 4 hours apart, to minimize damage to gastrointestinal and pulmonary cells. Bone marrow cells were isolated from donor femurs, and 0.5~1 x 10⁷ bone marrow cells in 100 µl PBS were adoptively transferred through the tail vein or retroorbital injection into irradiated recipient mice. Six to eight weeks post-transplantation, recipient mice were used for experiments.

Partial thickness wound

Mice were wounded in telogen. Briefly, mice were shaved, hair was removed using depilatory cream, and a Dremel drill head was used to gently scrape the back skin of anesthetized mice. To standardize the wound depth, the number of touches performed with the Dremel drill was determined by inspecting the wounded skin for the first signs of erythema and pinpoint bleeding. This method removes the epidermis and upper HF, including most infundibulum and isthmus cells, but leaves the HF bulge intact.

Flow Cytometry

To isolate single cell suspensions from wounded skin for analysis or sorting, the wound was placed in cold PBS for 15 minutes to remove the scab. The remainder of the wounded tissue was minced in digestion media: RPMI (Thermo Fisher) with HEPES (1:40, Thermo Fisher), MEM 100X (1:100, Thermo Fisher), sodium pyruvate (1:100, Thermo Fisher), penicillin/streptomycin (100 units/ml), gentamicin (1:500, Thermo Fisher), β-mercaptoethanol (1:1000). The tissue was digested with Liberase (25 µg/ml) (Roche) for 120 minutes at 37 °C with an adapted protocol.⁴ Single-cell suspensions were obtained, and cells were stained using an antibody cocktail prepared at predetermined concentrations in a staining buffer (PBS with 5% FBS and 1% HEPES). For immune profiling of the wound, fixable Live/Dead Cell Stain Kit was used to exclude dead cells. Stained cells were analyzed with BD Fortessa and LSR II Analyzer (BD Biosciences). The data were analyzed by FlowJo software and the number of various immune populations were calculated and normalized as “immune cell number per wound” for quantifying immune cells only in wounds or “immune cell number per cm²” for comparing immune cell numbers between unwounded and wounded skin. For RNA-seq and ATAC-seq, the single-cell suspensions were sorted after adding DAPI on BD FACSAriaII SORP running BD FACSDiva software.

To isolate HFSCs for in vitro co-culture assay, the back skins of WT C57/BL6J, *Cd80*^{-/-} and MHCII- mice were dissected and scraped with a blunt scalpel to remove excess fat. Skin was placed with the dermal side down in 0.25% trypsin/EDTA for 30 minutes. A single cell suspension was prepared and stained with antibody cocktail and HFSCs were sorted after adding DAPI. To FACS analysis of the CD80 expression levels on HFSCs post in utero injection, the single cell suspensions were isolated from the back skins of *Krt14Cre; Rosa26-LSL-Cas9* or *Rosa26-LSL-Cas9* mice whose skin epithelium had been specifically transduced with sgRNA. To obtain CD4⁺GFP⁻CD44^{Hi}CD62L^{Low} T cells for in vitro co-culture, the skin draining lymph nodes were collected from Foxp3-GFP/DTR mice on day2 post-wounding.

Immunofluorescence and RNA scope staining

Wounded and unwounded skin were fixed in 1% paraformaldehyde immediately after dissection for 1 hour at 4 °C and washed thrice in PBS. The tissue was incubated in 30% sucrose in PBS at 4 °C overnight. Tissue was then embedded in OCT (Tissue Tek), frozen, and sectioned (12-20um). Cryosections were permeabilized, blocked, and stained with the following primary antibodies: K10 (Rabbit, 1:1000, Biolegend), K14 (Chicken, 1:1000, Biolegend), mCD80 (Goat, 1:50, R&D), GFP (Rabbit, 1:1000, Abcam), Ly6G (Rat, 1:500, Biolegend), integrin α5 (Rat, 1:100, BD). The slides were then stained with secondary antibodies conjugated with Alexa Fluor 488, Alexa Fluor 647 and Rhodamine Red-X (Jackson ImmunoResearch Laboratories) and imaged on Zeiss Axio Observer Z1 equipped with ApoTome.2 or Leica Stellaris 8 Laser Scanning Confocal microscope. For the RNA scope staining, cryosections were dehydrated, performed with hydrogen peroxide and Protease III, hybridized with AMPs and developed the HRP-C1 channel with the *Cxcl5* probe according to the RNAscope Multiplex Fluorescent Reagent Kit Assay (ACDbio). Immediately after RNA labeling, the cryosections were stained with the primary antibody against K14 and the related secondary antibody. The images were collected by Leica Stellaris 8 Confocal microscope and analyzed using Fiji/ImageJ software.

Electron Microscopy

Skin samples were fixed in 2% glutaraldehyde, 4% PFA, and 2 mM CaCl₂ in 0.1 M sodium cacodylate buffer (pH 7.2) for over 1 hour at room temperature, post-fixed in 1% osmium tetroxide, and processed for Eponate 12 embedding. Ultrathin sections (60–65 nm) were counterstained with uranyl acetate and lead citrate. Images were taken with a transmission electron microscope (Tecnai G2-12; FEI) equipped with a digital camera (BioSprint29, Advanced Microscopy Techniques).

In vitro co-culture

FACS-sorted WT, *Cd80*^{-/-}, and MHCII- HFSCs were cultured on mitomycin C-treated feeders in Y medium with 650 µM calcium. Naïve CD4 T cells were isolated from the spleen of WT C57/BL6J mice using MojoSort Mouse CD4 Naïve T cell Isolation Kit (Biolegend). The purified naïve CD4 T cells were activated with 5 µg/mL pre-coated anti-CD3 and 5 µg/mL soluble anti-CD28 antibody (Thermo Fisher) for 72 hours in the presence of 10 ng/mL IL2. GFP^{neg}CD62L^{Low}CD44^{Hi} CD4 T cells or Treg cells were sorted from the lymph nodes of wounded Foxp3-GFP/DTR mice on day 2 post-wounding. 5 × 10⁴ CD3/CD28 pre-activated T cells, GFP^{neg}CD62L^{Low}CD44^{Hi} CD4 T cells or Treg cells were co-cultured with 5 × 10⁴ HFSCs in T cell media supplemented with 10 ng/mL IL2 and 10 ng/mL TGFβ for 3 days or 5 days. To co-culture HFSCs with OTII T cells, HFSCs were cultured in Y media with 650 µM calcium containing 15 µg/mL DQ-ovalbumin (Thermo Fisher, DQ-OVA) or 15 µg/mL ovalbumin peptide (InvivoGen, OVA323-339) at 37 °C for 72 hours. FACS-sorted CD11c+CD11b+ dendritic cells were cultured in T cell media with DQ-OVA or OVA323-339 at 37 °C for 24 hours as controls. 5 × 10⁴ OVA-loaded HFSCs and 5 × 10³ OVA-loaded dendritic cells were harvested by washing with PBS for three times, followed by co-culture with 5 × 10⁴ naïve CD4 T cells isolated from OTII mice in T cell media with 10 ng/mL IL2 and 10 ng/mL TGFβ for 5 days. Following the co-culture, Foxp3+ T cells were analyzed by flow cytometry.

RNA isolation and sequencing library preparation

Total RNAs from FACS-sorted epithelial cells were extracted using TRIzol (Invitrogen) followed by DNase I treatment and cleanup using the Direct-zol RNA Miniprep Kit (Zymo Research) following the manufacturer protocol. RNA-seq libraries were prepared with the NEBNext Single Cell/Low input RNA library prep kit for Illumina (NEB) following the manufacturer protocol. For sequencing, the Illumina Novaseq platform was used.

ATAC-Seq library preparation

ATAC-Seq libraries were generated from FACS-sorted tdTomato⁺ HFSCs using a previously described protocol with minor modifications.⁴⁹ Briefly, sorted cells were washed in 1xPBS, pelleted, and resuspended in an ice-cold lysis buffer (10mM Tris-HCl (pH 7.4), 3 mM MgCl₂, 10 mM NaCl, 0.1% IGEPAL). Following centrifugation and removal of lysis buffer, samples were subjected to the transposase reaction for 30min at 37C using 10ul of transposase enzyme (Illumina Tegment DNA Enzyme and Buffer kits). Transposed DNA was cleaned up using a Qiagen MiniElute PCR Purification Kit and amplified using 10-15 cycles. Libraries were sequenced using Illumina Novaseq sequencing platform.

Next generation sequencing data analysis**RNA-Seq Alignment and Differential Expression Analysis**

Raw sequenced reads were first trimmed and filtered by cutadapt (v3.2).³⁸ Estimated transcript counts for the mouse genome assembly GRCm38 (mm10, GENCODE vM24) were obtained using the pseudo-aligner Kallisto (v0.44.0).³⁹ Transcript-level abundance was summarized into gene level and differential gene expression was performed using the DESeq2 R package (v1.30.0) in R (v4.0.1).⁴⁰ Genes with absolute log₂ fold change > 2 and Benjamini-Hochberg method adjusted P values < 0.05 were regarded as significantly differentially expressed.

Gene Set Enrichment Analysis (GSEA)

GSEA was performed by clusterProfiler package (<https://guangchuangyu.github.io/software/clusterProfiler>) to calculate the overlap between a gene list and pathways in MSigDB (Molecular signature database, v7.4) gene set collections (<http://www.gsea-msigdb.org/gsea/msigdb/index.jsp>).⁴¹ Genes were ranked by the fold change value obtained from DESeq2. Pathways enriched with Benjamini-Hochberg method adjusted P values < 0.25 were considered to be significant.

ATAC-seq

Raw sequenced reads were first trimmed and filtered by cutadapt (v3.2). We then used Bowtie2 (v2.3.4.3) to map the clean reads to the mm10 reference genome and duplicates were removed using Picard (v2.18.7) (<http://broadinstitute.github.io/picard/>). ATAC-seq signal tracks were generated using deepTools and presented by Gviz package.⁴²⁻⁴⁴ Peaks were called using MACS2 (v2.2.7.1).⁴⁵ Peaks were then combined and merged in bedtools (v2.30.0).⁴⁶ Read counts were summed for each genomic region by featureCounts (v1.5.3).⁴⁷ DESeq2 was applied to identify the differentially accessible regions from ATAC-seq data.

Single cell RNA-seq

Gene-cell count matrices from different samples were downloaded from GSE142471.²⁶ Replicates for unwounded and wounded samples were merged using Seurat (v.4.1.0).⁴⁸ Cells with <200 detected genes or >5000 detected genes or > 7.5% mitochondrial genes were filtered-out from the dataset. Then data were column-normalized and log-transformed. All replicates were integrated using reciprocal PCA method. To identify cell clusters, principal component analysis (PCA) was first performed and the top 30 PCs with a resolution = 0.4 were applied. Non-immune cells were subset based on the expression of CD45 (Ptprc) and re-clustered using the same parameters.

Statistics

Statistical analysis for microscopy quantifications was performed in Prism 9 (GraphPad). Column data were first analyzed using D'Agostino and Pearson normality testing. The two-tailed Mann-Whitney test was performed for data not normally distributed with a 95% confidence interval. The unpaired two-tailed student's t-test was performed for normally distributed data with a 95% confidence interval. Data are presented as mean \pm SEM. Significant differences between groups were noted by asterisks (* p<0.05; ** p<0.01, *** p<0.001, **** p<0.0001). The group size was determined by power analysis based on preliminary experimental results. Experiments were performed unblinded.

Data and Software Availability

Raw and analyzed data is available at NCBI and the accession number for the RNA sequencing and ATAC-seq data reported in this paper are NCBI GEO: GSE220241.